Technical Report

TR-09-02

Mineralogical investigations of the interaction between iron corrosion products and bentonite from the NF-PRO Experiments (Phase 1)

A E Milodowski, M R Cave, S J Kemp, H Taylor,
B P Vickers, K A Green, C L Williams, R A Shaw

British Geological Survey

January 2009

Svensk Kärnbränslehantering AB
Swedish Nuclear Fuel
and Waste Management Co

Box 250, SE-101 24 Stockholm
Phone +46 8 459 84 00

SKB

Mineralogical investigations of the interaction between iron corrosion products and bentonite from the NF-PRO Experiments (Phase 1)

A E Milodowski, M R Cave, S J Kemp, H Taylor,
B P Vickers, K A Green, C L Williams, R A Shaw

British Geological Survey

January 2009

Keywords: Iron corrosion, Radioactive waste, Spent fuel, Bentonite, Smectite, Chlorite, Iron oxides, Aragonite, Ion exchange, Exchangeable cations.

Foreword

This report is the published product of a study by the British Geological Survey (BGS) commissioned by the Svensk Kärnbränslehantering AB (SKB) to provide background mineralogical information for laboratory experiments on the interaction between iron corrosion products and bentonite, undertaken on behalf of SKB by Serco Assurance as part of European Union Framework VI project NF-PRO /Smart et al. 2006/. The purpose of the BGS investigations was to determine whether or not there is evidence for clay mineral alteration by Fe within the bentonite, and the results will be used to help guide the future characterisation of experimental residues from further Serco Assurance experiments that are currently in progress.

Acknowledgements

Dr Nick Smart (Serco Assurance) is acknowledged for providing background information on the experimental studies and helpful discussions on the interpretation of the data. Dr Lars Werme (SKB) and Dr Virginia Oversby are also thanked for their support and encouragement during the project and for their helpful review of this report.

Summary

This report summarises the findings of a programme of work under taken by the British Geological Survey (BGS) on behalf of Svensk Kärnbränslehantering AB (SKB), to characterise the mineralogical alteration of compacted bentonite from experiments designed to study the interaction between iron corrosion and bentonite. The experiments were undertaken by Serco Assurance (Culham Laboratory, Oxfordshire, United Kingdom), and were co-funded by SKB within the EU Framework 6 NF-PRO Project /Smart et al. 2006/.

Reacted bentonite residues from three NF-PRO Experiments – NFC12, NFC16 and NFC17 were examined by BGS using; X-ray diffraction analysis (XRD); petrographical analysis with backscattered scanning electron microscopy (BSEM) and energy-dispersive X-ray microanalysis (EDXA) techniques, cation exchange capacity (CEC) and exchangeable cation analysis; and sequential chemical extraction.

Bentonite immediately adjacent to corroding steel was found to have interacted with Fe released from the corroding metal. This resulted in the formation of narrow haloes of altered bentonite around the corroding steel wires, in which the clay matrix was significantly enriched in Fe. Detailed petrographical observation found no evidence for the formation of discrete iron oxide or iron oxyhydroxide phases within the clay matrix but appeared to show that the clay particles themselves had become enriched in Fe. XRD observations indicated a slight increase in d_{002}/d_{003} peak ratio, which could possibly be accounted for by a small amount of substitution of Fe into the octahedral layers of the montmorillonite. If correct, then this alteration might represent the early stages of conversion of the dioctahedral montmorillonite to an iron-rich dioctahedral smectite such as nontronite. Alternatively, the same effect may have been produced as a result of the displacement of exchangeable interlayer cations by Fe and subsequent conversion to form additional Fe-rich octahedral layers. In either case, the XRD results are consistent with the petrographical observations, potentially indicating the early stages of conversion of montmorillonite towards an iron-rich clay mineral as a result of interaction with Fe released by the corrosion of iron or steel.

The cation exchange capacity (CEC) and exchangeable cation chemistry of the bentonite was also seen to be subtly affected by interaction with Fe. Bentonite from within the zones where corroded steel wires were present displayed a slightly reduced CEC, and depletion in exchangeable Ca and Na, and an increase in exchangeable Fe. This is consistent with at least partial displacement of the interlayer cations in montmorillonite by Fe. The loss in CEC might also correlate with a partial conversion of the montmorillonite to chlorite, which is tentatively suggested from the XRD analyses.

Fe released from the corroding steel was also observed to displace Ca^{2+} from the interlayer cation sites in the montmorillonite component. This was manifested by the marked concentration of Ca at the interface with the corroding metal and along the leading edges of 'fronts' of Fe diffusing into the bentonite matrix. The displaced Ca was seen to have re-precipitated as aragonite.

The petrographical observations show that the bentonite within the alteration zone, that has reacted with and is enriched by Fe, has a tendency to show significantly reduced shrinkage on sample drying in comparison to the background unaltered bentonite. Conversely, this would suggest that the reacted and altered clay will also have less ability to swell on hydration with water. This behaviour might be consistent with the partial conversion of the montmorillonite to an iron rich dioctahedral smectite such as nontronite, or to non-swelling clay mineral such as chlorite (or chlorite-smectite mixed-layer clay). If this is the case, then this may have important implications for the long-term behaviour of bentonite seals around radioactive waste canisters made of iron or steel.

Contents

1 Introduction 9

2 The iron-bentonite interaction experiment samples 11

3 **Analytical methods** 13
3.1 Petrographical analysis 13
3.1.1 Polished section preparation 13
3.1.2 Backscattered scanning electron microscopy 13
3.2 X-ray diffraction analysis 14
3.2.1 Sample preparation 14
3.2.2 Analysis 15
3.2.3 Clay mineral modelling 15
3.3 Cation exchange capacity and exchangeable cation analysis 15
3.4 Sequential chemical extraction analysis 15
3.4.1 Extraction procedure 16
3.4.2 Chemical analysis 16

4 Results 17
4.1 Petrographical observations 17
4.1.1 Experiment NFC12 17
4.1.2 Experiment NFC16 25
4.1.3 Experiment NFC 17 30
4.2 X-ray diffraction analysis 35
4.2.1 Unaltered background bentonite 35
4.2.2 Altered bentonite adjacent to corroded steel wire and iron coupon 37
4.3 Cation exchange and exchangeable cation characteristics 42
4.4 Sequential chemical extraction analysis 44
4.4.1 Data processing 44

5 Discussions and conclusions 49
5.1 Background mineralogical characteristics of MX-80 bentonite 49
5.2 Bentonite alteration characteristics 49
5.2.1 Clay mineral alteration 49
5.2.2 Other mineralogical alteration 51
5.2.3 Change in cation exchange properties 52
5.2.4 Bentonite shrinkage and swelling characteristics 52
5.3 Steel corrosion 53

References 55

1 Introduction

The Svensk Kärnbränslehantering AB (SKB) disposal concept for the disposal of spent fuel and high-level radioactive waste considers using a system that consists of a copper-clad iron waste canister that is surrounded by bentonite clay, and emplaced within an underground repository located in crystalline basement rocks. The canister and the bentonite act as the engineered barrier that is designed to prevent the release of radionuclides into the biosphere. Initially, the disposal concept design was for emplacement of the canisters and bentonite over-pack within vertical disposal holes drilled within the galleries of an underground repository in granitic host rocks. More recently consideration has also been given to emplacement within horizontally drilled boreholes, which has advantages with respect to reducing the size and height that is required in the excavated repository galleries. However, emplacement in horizontal disposal holes requires a steel 'cage' to be used to hold the bentonite blocks in place around the canister, and to provide strength to prevent deformation of the canister, during its emplacement.

One aspect of concern, regarding the long-term stability and integrity of the barrier system, is the effect of possible interactions that might occur between the iron and steel components and the bentonite buffer material. Of particular concern are whether or not the bentonite might enhance iron corrosion, and whether or not the oxidation of iron and its iron corrosion products might interact with the bentonite, thereby altering its swelling/sealing, ion exchange, sorption and radionuclide retardation properties. Potentially important changes that might be expected in bentonite as a result of interaction with iron and its corrosion products include:

- Substitution of interlayer cations such as Na^{+} and Ca^{2+} in the smectite component by Fe^{2+} produced by iron corrosion /Kamei et al. 1999, Idemitsu et al. 2003/;
- Reduction of Fe^{3+} in octahedral structural site in the smectite clay mineral component by the oxidation of the adjacent metallic iron /Stuki et al. 1984, Kostka et al. 1999/;
- Alteration (transformation) of smectite to an Fe-rich clay mineral such as mixed-layer chlorite-smectite or chlorite /e.g. Wilson et al. 2006a,b/.

In order to investigate these problems, the SKB have co-funded an experimental study by Serco Assurance (Culham Laboratory, Oxfordshire, United Kingdom) to investigate the interaction of iron and bentonite, within the EU Framework 6 NF-PRO Project /Smart et al. 2006/. Initial results from the Serco Assurance experiments have indicated higher than expected rates of iron corrosion, and significant increases in Fe content have been identified in the bentonite in contact with the corroding iron. However, the analyses of the experimental residues have been inconclusive in regard to either (i) the reason for the enhanced corrosion; (ii) the nature of the Fe enhancement in the bentonite, or; (iii) evidence for any alteration or transformation of the smectite clay mineral component to an Fe-rich phase. Consequently, the British Geological Survey (BGS) was requested by SKB (Dr Lars Werme) to undertake a programme of specialist mineralogical analyses to characterise the clay mineralogy and determine the iron distribution characteristics within the reacted bentonite residues from three of the Serco Assurance experiments that have been completed to date. The purpose of the BGS investigations was to determine whether or not there is evidence for clay mineral alteration by Fe within the bentonite. The results will be used to help guide the future characterisation of experimental residues from further Serco Assurance experiments that are currently in progress.

2 The iron-bentonite interaction experiment samples

The experimental system of the bentonite-iron interaction experiments conducted by Serco Assurance is described by /Smart et al. 2006/. It consists of a series of experimental cells consisting of a composite cylinder of compacted bentonite containing iron coupons and steel wires loaded into a stainless steel holder, which was designed to allow artificial groundwater to enter the bentonite and gas to escape, by means of porous sintered metal filters (gas permeable) placed within a stainless steel pressure vessel (cf. Figure 1 in /Smart et al. 2006/). The composite bentonite cylinders used in the experiments comprised two discrete components (illustrated schematically in Figure 2-1):

- A central region consisting of MX-80 bentonite dry mixed with carbon steel wires (5 mm in length, 0.45 mm diameter), then compressed to form a short cylinder. This was sandwiched between:
- An outer region of compacted MX-80 bentonite at either end of the composite cylinder, containing a flat coupon of iron.

The composition of the steel wires used in the experiments is reported by /Smart et al. 2006/ as BS4360 grade 43A (EN1024B-1) carbon steel (composition wt % C 0.21; Si 0.220; Mn 0.7; S 0.017; P 0.017, balance = Fe).

The experiments were conducted in an oxygen-free nitrogen-flushed glove box to study iron corrosion under a reducing environment. The experimental conditions for the reacted bentonite from the three cells examined in this study are given in Table 2-1 (data provided by Dr NR Smart, Serco Assurance).

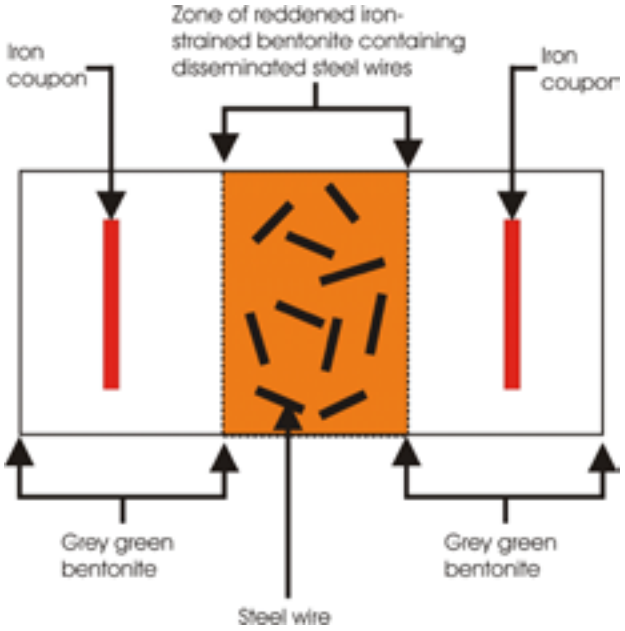

Figure 2-1. *Schematic illustrating the different parts of the compacted bentonite-iron composite from the Serco Assurance NF-PRO experimental cells after reaction.*

Table 2-1. Summary of operating conditions for the NF-PRO experiments.

Experiment	Fluid	Temp. (°C)	pH	Start Date	End Date	Exposure Time (days)
NFC12	1M NaCl	50	11	18/8/2005	25/11/2005	99.0
NFC16	1M NaCl	50	8.4	27/8/2005	08/3/2006	193.0
NFC17	1M NaCl	50	8.4	27/8/2005	13/3/2006	198.0

Three of the experimental runs (Serco Assurance experiments NFC12, NFC16 and NFC17) were selected for the present study. The vessels were opened and sampled within a nitrogen-purged glove-box to exclude oxygen. Reference photographs were taken of the reacted bentonite prior to sampling. Samples were then taken from selected parts of each cylinder by cutting the soft bentonite with a sharp knife. These samples were then sealed into crimp-welded plastic bags (triple bagged), which were filled with oxygen-free nitrogen inside the glove-box. All sampling was carried out by Serco Assurance at Culham Laboratory, and the sealed sub-samples were then passed on to the BGS for mineralogical analysis.

All three experiments displayed obvious reddish-brown staining of the central region of the bentonite cylinder that was associated with the corrosion of the disseminated steel wires (cf. Figure 2-1). Since the remit of the BGS investigations was to focus on the potential alteration of the bentonite by interaction with iron corrosion products, the BGS sub-samples were selected principally from the central region of bentonite containing disseminated steel wires, which visually displayed the greatest apparent alteration. Sub-samples were selected from the middle of the zone containing disseminated steel wires and from the interface between the iron-stained central region and adjacent unstained bentonite. Since no unreacted MX-80 bentonite starting material was available for comparison, apparently unaltered compacted bentonite from the distal ends of the cylinders from experiments NFC12 and NFC17 was also sampled to provide 'background' reference material for comparison with bentonite from the central region of the reacted bentonite cylinders. Details of the samples taken for analysis are summarised in Table 2-2.

Table 2-2. Summary description of sub-samples examined from the NF-PRO experiments.

SERCO Experiment	SERCO Sample Code	BGS Sample Code	Description
NFC12	12a	MPLM561	Grey-green bentonite disc: background material from end of experimental cell, with iron corrosion products on one side due to contact with iron coupon
	12b	MPLM562	Bentonite from interface region between 'bentonite-steel wire zone' and 'iron-free bentonite zone': part grey-green, part with steel wires and pervasively stained with iron corrosion products
	12c	MPLM563	Bentonite with steel wires from centre of 'bentonite-steel wire zone', pervasively stained with iron corrosion products
NFC16	16a	MPLM565	Bentonite from interface region between 'bentonite-steel wire zone' and 'iron-free bentonite zone': half grey-green, half with steel wires and pervasively stained with iron corrosion products
	16b	MPLM566	Bentonite with steel wires from centre of 'bentonite-steel wire zone', pervasively stained with iron corrosion products
NFC17	17a	MPLM567	Bentonite from interface region between 'bentonite-steel wire zone' and 'iron-free bentonite zone': with steel wires and pervasively stained with iron corrosion products on one side
	17b	MPLM568	Grey-green bentonite disc: background material from end of experimental cell and not associated with any iron corrosion products
	17c	MPLM569	Bentonite with steel wires from centre of 'bentonite-steel wire zone', pervasively stained with iron corrosion products

3 Analytical methods

The sub-samples of reacted bentonite from NF-PRO experiments NFC12, NFC16 and NFC17 were provided by Serco Assurance in a moist state, preserved within heat-sealed plastic bags filled with oxygen-free nitrogen. These were opened and rapidly transferred to an Edwards Modulyo vacuum freeze drying unit and which was then immediately pumped down to vacuum to minimise exposure to air, thereby minimising the risk of oxidation of any ferrous iron phases. The samples were then left to dry for 72 hours under vacuum, after which they were stored under vacuum until required to be sub-sampled for analysis.

The total amount of material that was available from the experimental cells for mineralogical characterisation was very limited because of the need to undertake several types of analysis. In addition, because the intention was to examine mineralogical differences between sub-samples of the bentonite taken from different regions in the cells the mass of material that could be used for each analytical technique was further reduced.

3.1 Petrographical analysis

Petrographical analysis focussed on observing the interaction of bentonite with iron and any associated alteration effects immediately adjacent to the corroding steel wires within the thin 'zone of reddened iron stained bentonite containing disseminated steel wires' from within the centre of the compacted bentonite-iron composite (Figure 2-1) used in the NF-PRO experiments. Samples were then examined in polished thin section using backscattered scanning electron microscopy (BSEM), after initial examination by petrological microscope (in transmitted light). Image brightness in BSEM images is related to the average atomic number of the phases observed /Goldstein et al. 1981/, and this therefore allows differentiation of the different minerals present. Element distributions in the bentonite matrix surrounding corroded steel wires were also studied by using digital energy-dispersive X-ray microanalysis (EDXA) elemental mapping.

3.1.1 Polished section preparation

Intact vacuum-dried fragments of this material, approximately 20×10 mm were impregnated with epoxy-resin under vacuum in order to stabilise the material for polished section preparation. These resin-impregnated blocks were then cut and polished under paraffin (to prevent reaction of the smectite with water-based cutting fluids) to produce polished thin sections 30 μm thick bonded onto 45×28 mm glass microscope slides with a colourless epoxy-resin. A blue dye was added to the epoxy-resin prior to vacuum impregnation to differentiate between porosity originally present within the vacuum-dried sample and artefacts of the sectioning process (e.g. grain plucking), when subsequently observed by transmitted-light microscopy. The sections were finished by polishing with 0.45 μm diamond paste.

3.1.2 Backscattered scanning electron microscopy

BSEM was carried out using a LEO 435VP variable pressure digital scanning electron microscope fitted with a solid-state 4-element (diode) backscattered electron detector, and equipped with an Oxford Instruments INCA EDXA system with a thin window Si-Li X-ray detector capable of detecting elements from boron to uranium. The scanning electron microscope instrument was operated in the conventional high vacuum mode ($<1\times10^{-4}$ torr), using a 10–20 kV electron beam accelerating potential, beam currents between 200–800 pA, and a working distance of 17–20 mm, as required. Phase identification was aided by microchemical information obtained

from observation of semi-quantitative EDXA spectra recorded from features of interest. Digital EDXA X-ray element maps were recorded from selected areas of interest, using a 20 kV electron beam, 200–400 pA beam currents and at a working distance of 19 mm. EDXA spectra and digital X-ray elemental maps were processed using the INCA Suite Version 4.08 (2006) software package. X-ray element maps were typically produced by summation of data recorded from 30–100 frame scans recorded over 45–120 minutes. Images were processed to show relative element concentrations using a 'rainbow colour scale' ranging from blue (representing zero background) through green, yellow and orange (low to intermediate concentration) to red or white (representing high concentration).

X-ray elemental maps were recorded for:

- C and Cl which gives an indication of where epoxy-resin impregnates the samples. Cl might also indicate where residual sodium chloride pore fluid has deposited salt on drying;
- Si, Al, and Mg, which will be derived from the silicate mineral assemblage of the bentonite;
- Na, K, and Ca, which will be derived largely from the exchangeable cation component of the smectite clay mineral that dominates the bentonite. K and Na will also be recorded from minor amounts of K-feldspar, albite and zeolites that may also be present in the bentonite. Ca also reveals the presence of any minor calcium carbonate (aragonite or calcite) that may be present. Mg might also be present within the exchangeable cation sites in the smectite. Na concentration might also be indicative of salt deposited from drying of any residual pore fluid;
- Fe maps primarily record the location of the steel wires and any Fe-rich alteration products. Accessory Fe-bearing minerals such as pyrite and natural iron oxides (ilmenite, magnetite) will also be shown in the Fe maps;
- Maps for P and Mn were also recorded.

3.2 X-ray diffraction analysis

3.2.1 Sample preparation

Due to the very small size of the sample material available for analysis from the experiments and nature of the regions of the samples to be analysed, 'zero-background' silicon crystal substrate X-ray diffraction (XRD) mounts were used rather than the standard cavity XRD sample holders or ceramic tiles which require greater volumes of sample.

Firstly, in order to study the mineralogy of the samples as supplied and to prevent further oxidation of any Fe-bearing species, small (typically c.10 mg) portions of material were rapidly removed using a scalpel. Any steel wire remaining in these sub-samples was removed using a hand magnet before grinding the material to a fine powder in an agate pestle and mortar. The powder was then deposited onto the surface of the silicon crystal substrate using a single drop of acetone to form a random orientation. Such analyses were carried out to determine the nature of any non-clay minerals present in the samples and also to determine the d_{060} spacing of any clay minerals present.

Secondly, the clay mineral assemblages of the samples were studied by preparing oriented mounts. Typically, such analyses would be initiated by the isolation of a fine, <2 μm size fraction to increase the concentration of clay minerals. However in this case, clay minerals form >75% of the MX-80 bentonite starting material /Madsen 1998/ and therefore any such concentration is unnecessary. In addition, size separation of sodium bentonites is typically difficult as they form colloidal gels in water. Any requirement for the addition of a dispersing agent (typically sodium hexametaphosphate, 'Calgon') would also alter the exchangeable cation chemistry of the bentonite and its XRD characteristics. Therefore in this study, material for oriented XRD mounts was prepared by dispersing small (typically c.10 mg) portions of material in deionised water using ultrasound treatment and no dispersant was added. The dispersions

were then pipetted onto ‘zero-background’ silicon crystal substrates and allowed to dry at room temperature.

3.2.2 Analysis

XRD analysis was carried out using a PANalytical X’Pert Pro series diffractometer equipped with a cobalt-target tube, X’Celerator detector and operated at 45 kV and 40 mA.

The random powder mounts were scanned from 4.5–85°2θ at 2.76°2θ/minute. Diffraction data were initially analysed using PANalytical X’Pert Highscore Plus version 2.2a software coupled to the latest version of the International Centre for Diffraction Data (ICDD) database.

The oriented mounts were scanned from 2–40°2θ at 1°2θ/minute after air-drying, after glycol-solvation and after heating to 550°C for 2 hours.

3.2.3 Clay mineral modelling

In order to gain further information about the nature of the clay minerals present in the samples, modelling of the XRD profiles was carried out using Newmod-for-Windows™ /Reynolds and Reynolds 1996/ software. Modelling was also used to assess the relative proportions of clay minerals present by comparison of sample XRD traces with Newmod-for-Windows™ modelled profiles. The modelling process requires the input of diffractometer, scan parameters and a quartz intensity factor (instrumental conditions), and the selection of different sheet compositions and chemistries. In addition, an estimate of the crystallite size distribution of the species may be determined by comparing peak profiles of calculated diffraction profiles with experimental data. By modelling the individual clay mineral species in this way, mineral *‘reference intensities’* were established and used for quantitative standardization following the method outlined in /Moore and Reynolds 1997/.

3.3 Cation exchange capacity and exchangeable cation analysis

The cation exchange capacity (CEC) was determined using the technique based on the compulsive exchange between an aqueous solution of magnesium sulphate and a barium soil /Bascomb 1964/. This method is routinely used in the analysis of rocks and soils for environmental assessment /Gillespie et al. 2000a,b, 2001/. The samples were shaken with two separate portions of barium chloride solution, buffered at pH 8.1 with triethanolamine, and then washed with water to remove any excess barium chloride. Magnesium sulphate solution was then added to the barium-saturated materials to displace the barium, which was precipitated as insoluble barium sulphate. The amount of magnesium exchanged was then determined by titrating the excess magnesium sulphate with EDTA.

Exchangeable cations were determined on the $BaCl_2$/triethanolamine extractant by inductively-coupled plasma – atomic emission spectroscopy (ICP-AES), and checked against matrix matched standards. The cation species determined by ICP-AES included Ca, Mg, Na, K and Fe.

3.4 Sequential chemical extraction analysis

The chemical partitioning of iron between the different ‘mineral phases’ in the reacted bentonite was explored further by using sequential chemical extraction. The sequential extraction methodology used was the ‘Chemometric Identification of Mineral Substrates and Element Distributions (CISED) Test’ /Cave et al. 2004/, which is based on the chemometric data interpretation of a series of 14 solutions (involving 2 replicates for each of 7 leachant stages) derived from the extraction of solutes using separate aliquots of Aqua Regia of increasing concentration.

3.4.1 Extraction procedure

Approximately 0.2 g of subsampled bentonite experimental residue was accurately weighed into 8 ml Sterilin plastic containers and 4 ml of the starting leachant (de-ionised water) was added. The container was mounted on an end-over-end shaker for 5–10 minutes, allowing the leachant and the sample to mix. The unit was then centrifuged for 5 minutes, or until separated, at 3,000 rpm. The surface leachate collected was then removed using a pipette for analysis by inductively-coupled plasma – atomic emission spectroscopy (ICP-AES), before the next leachant was added and the process was repeated. In addition, 0.1, 0.2, 0.3 and 0.4 ml, respectively, of hydrogen peroxide were added to leachates G/H, I/J, K/L and M/N before making up to volume. The sequence of leachants used is summarised in Table 3-1.

3.4.2 Chemical analysis

All extracts were analysed by ICP-AES at dilutions made using 1% HNO_3, except the blank extracts for which dilutions were made using de-ionised water. Detectable concentrations of some determinands were found in the procedural blank performed with the extractions, specifically Cr, Fe, Total P and Zn. Data have not been corrected for these blank concentrations.

Two of the extract solutions could not be analysed – Sample 16b (BGS sample MPLM566) extract fraction Duplicate A and Sample 17b (BGS sample MPLM568) extract fraction B – because the solutions were lost as a result of failure of the Sterilin containers and subsequent leakage on centrifugation during the extraction process.

Table 3-1. Summary details of the sequential extraction leachants used in the CISED test.

Leachate Fraction No.	Leachant solution
A/B	De-ionised water
C/D	0.01 M Aqua Regia
E/F	0.05 M Aqua Regia
G/H	0.1 M Aqua Regia
I/J	0.5 M Aqua Regia
K/L	1 M Aqua Regia
M/N	5 M Aqua Regia

4 Results

4.1 Petrographical observations

4.1.1 Experiment NFC12

General observations

Visual inspection of the cylinder of compacted bentonite recovered from Experiment NFC12 indicated that significant alteration and reaction had occurred within the central region containing the dispersed steel wires, as evident from the very strong red-brown staining of the bentonite within this region (Figure 4-1). The stained central region was between 25–30 mm wide, extending into the bentonite for up to about 5 mm from the margins of the zone containing the steel wires (Figure 4-2). Much of the reddish brown ferruginous staining was developed along a 'chicken wire mesh-like' network of interconnected hairline fractures within this central region, with extensive diffusive impregnation of the discolouration into the adjacent bentonite matrix. The fractures had a typical spacing of the order of 3–8 mm.

Closer examination of freshly broken fragments (after vacuum drying) taken from the corroded wire zone region of the bentonite cylinder showed that the surfaces of the steel wires were coated with a very thin film of very dark brown to black oxide corrosion product, surrounded by a halo of dark reddish-brown colouration of the adjacent bentonite that becomes a more diffuse and lighter orange to light reddish brown stain in the bentonite matrix beyond about 0.1–0.5 mm distance from the wire surface (Figure 4-3). Fragments of the dark brown to black oxide corrosion product display ferromagnetic properties and could be attracted to a strong hand magnet. A similar black corrosion product recovered from the surface of corroded wires in Experiment 17 was found by XRD analysis (see Section 4.2.2, Random orientation mount XRD) to contain magnetite [Fe_3O_4]. Therefore, it seems likely that the black oxide product seen on the surfaces of the corroded steel wires in Experiment NFC12 is probably also magnetite.

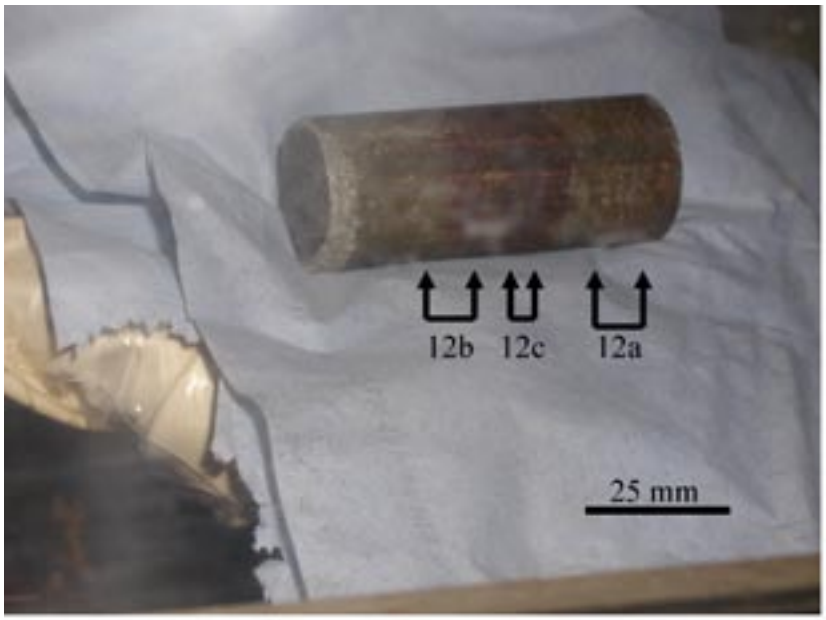

Figure 4-1. *Composite cylinder of compacted bentonite with steel wires and iron coupons recovered after experimentation from Experiment NFC12 (photographed in nitrogen filled glove box). The central region containing the corroded steel wires is strongly stained by reddish brown iron oxide alteration. Relatively fresh or unaltered grey-green bentonite remains at the end of the cylinder. The locations of subsamples taken for analysis are shown. [Photograph provided courtesy of Serco Assurance]*

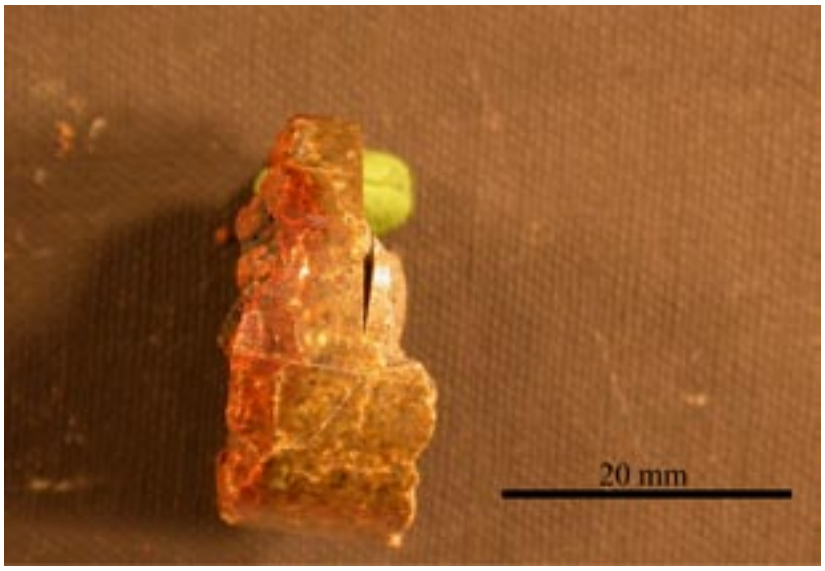

Figure 4-2. *Photograph of subsample 12b. The left hand edge of the sample contains embedded steel wires at the interface between the steel wire-bentonite zone and bentonite without steel wires. The reddish brown staining permeates for up to 5 mm from this interface into the adjacent bentonite. Experiment NFC12.*

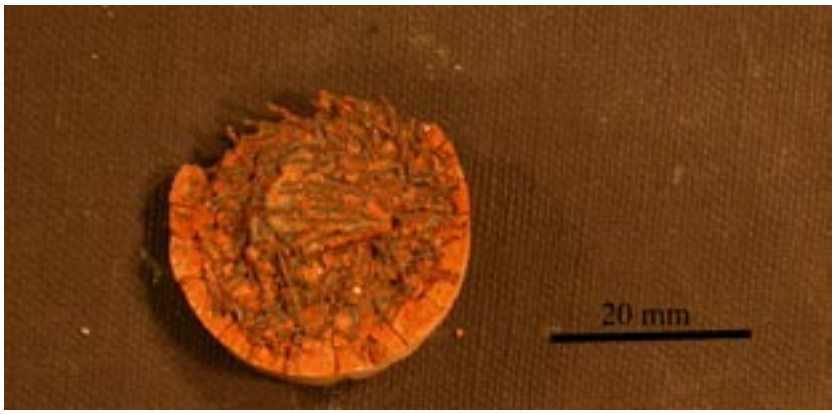

Figure 4-3. *Photograph of subsample 12c sliced from the centre of the steel wire region of the compacted bentonite. The corroded wire surfaces are coated with a black iron oxide corrosion product, surrounded by narrow haloes of reddish-brown iron oxide alteration product. The adjacent bentonite matrix is strongly stained orange-brown. Note that shrinkage and cracking of the bentonite has occurred around the wire-free margin of the slice, whereas, the centre of the disc contaminating the wires displays markedly less shrinkage cracking. Experiment NFC12.*

The region of the bentonite cylinder containing the iron coupons showed a weak orangey-coloured ferruginous discolouration of the grey green bentonite (as, for example, within the region indicated by sample 12a in Figure 4-1). Closer examination of freshly fractured slices through this region showed that the iron coupon was coated with a thin film of reddish brown iron oxide. Most of the 'iron staining' in the bentonite was seen to be limited to within 1–2 mm of the surface of the iron coupon with only very localised and limited iron staining further beyond this (Figure 4-4).

It was noticeable that the shrinkage behaviour of the bentonite matrix on drying was different between the heavy iron-stained central part of the steel wire-bearing region and the margins of the bentonite that were free of steel wires. The heavily iron-impregnated areas from the centre of the zone with abundant corroded steel wire displayed much less shrinkage and cracking after vacuum-drying than the margins of the zone that were free of corroded steel wires (Figure 4-3).

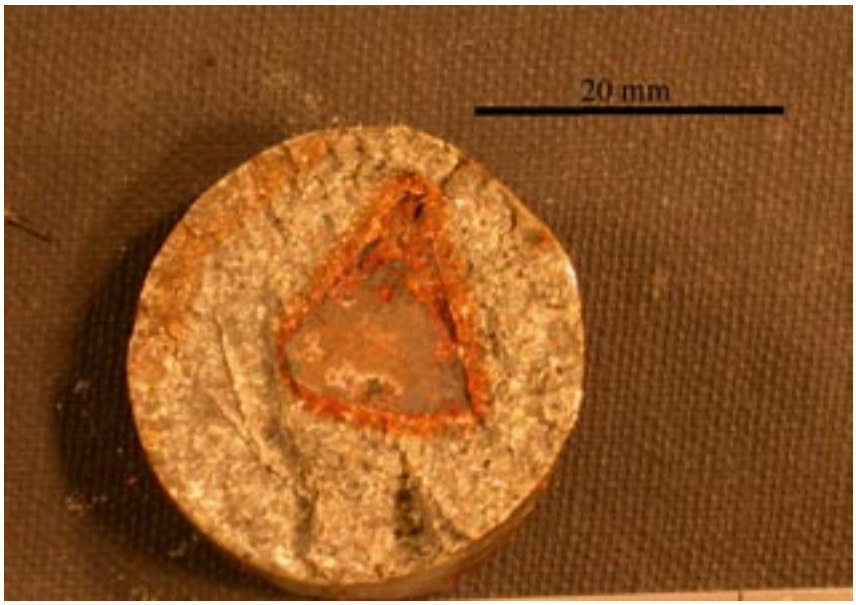

Figure 4-4. *Photograph of subsample 12a sliced through the contact of the iron coupon near the unaltered end of the compacted bentonite cylinder (iron coupon removed), showing the 'triangular' mouldic impression of the segment of iron coupon. The coupon surface is coated with a film of reddish-brown iron oxide corrosion product and surrounded by thin halo of reddish-brown iron oxide staining in the immediately adjacent bentonite. Localised weak staining by orange-brown alteration can be seen in the outer margins of the sliced bentonite disc. Experiment NFC12.*

Detailed petrography

Backscattered scanning electron microscopy (BSEM) of the polished thin section prepared through the zone of bentonite containing disseminated steel wires indicates that there has been significant reaction and corrosion of the steel wires, with the formation of a halo of alteration in the enclosing bentonite (e.g. Figure 4-5 and Figure 4-6). This halo shows up brighter than the background bentonite due to its significant impregnation with Fe, and as a result it has a higher average atomic number than the Na-Si-Al-dominated matrix of the unaltered bentonite, and consequently has a much higher backscattered electron coefficient (i.e. it is more 'reflective' to electrons). The halo of alteration products and altered bentonite around the corroded steel wires is generally between 50–100 µm thick but may be up to 250 µm thick in some cases. However, the impregnation of the bentonite by Fe may extend much further along microfractures radiating from around each of the altered wires (e.g. Figure 4-5 and Figure 4-6). These microfractures were observed penetrating the bentonite matrix for up to 1 mm from wire surface around some of the wires.

The surfaces of the steel wires were observed to be pitted and etched, with thin concentric bands of very fine grained secondary iron oxide or iron oxyhydroxide coating the corroded metal surface (Figure 4-7). XRD analyses (see Section 4.2.2, Random orientation mount XRD) tentatively suggest that this may be åkaganeite (β-FeO[OH, Cl]). This secondary iron oxide alteration either forms a structureless coating filling corrosion pits or appears to be highly microporous (e.g. Figure 4-7) and may display a microcellular structure containing residual corroded fragments of iron metal. The corrosion pits on some wires were seen locally to penetrate up to 20 µm deep into the metal, but in most cases the corrosion pitting is around 10 µm deep. Generally the thickness of the alteration halo around the corroded wire is greatest adjacent to where the wire is most extensively corroded.

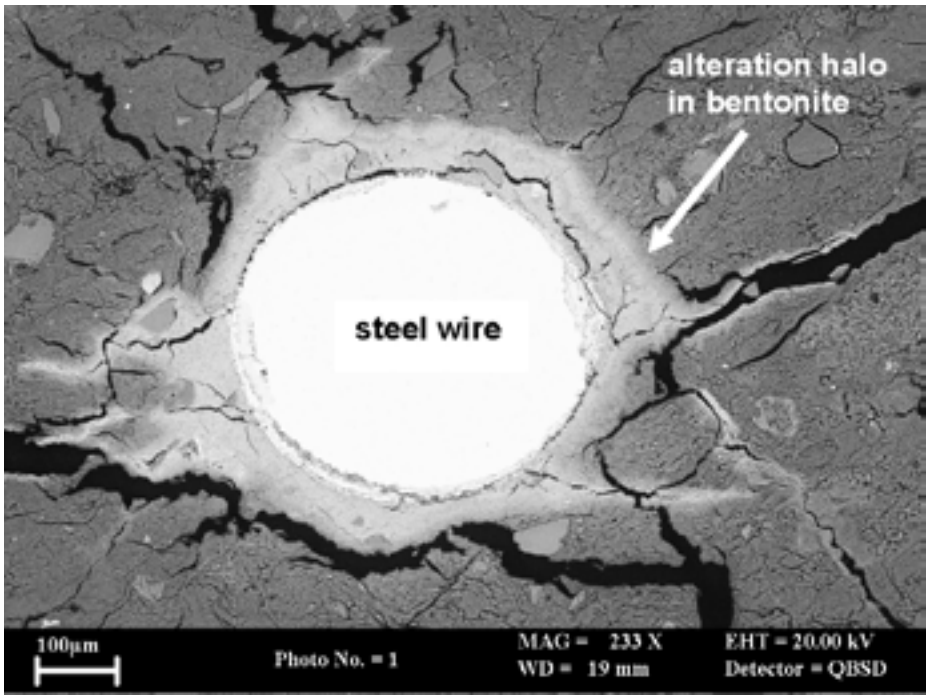

Figure 4-5. *BSEM photomicrograph of a corroded steel wire (white) in bentonite. The bentonite around the wire shows a halo of alteration (light grey) which also penetrates further into the bentonite clay matrix (darker grey) along microfractures. Disseminated angular grains of K-feldspar (mid grey) show no evidence of alteration. Experiment NFC12, subsample 12c.*

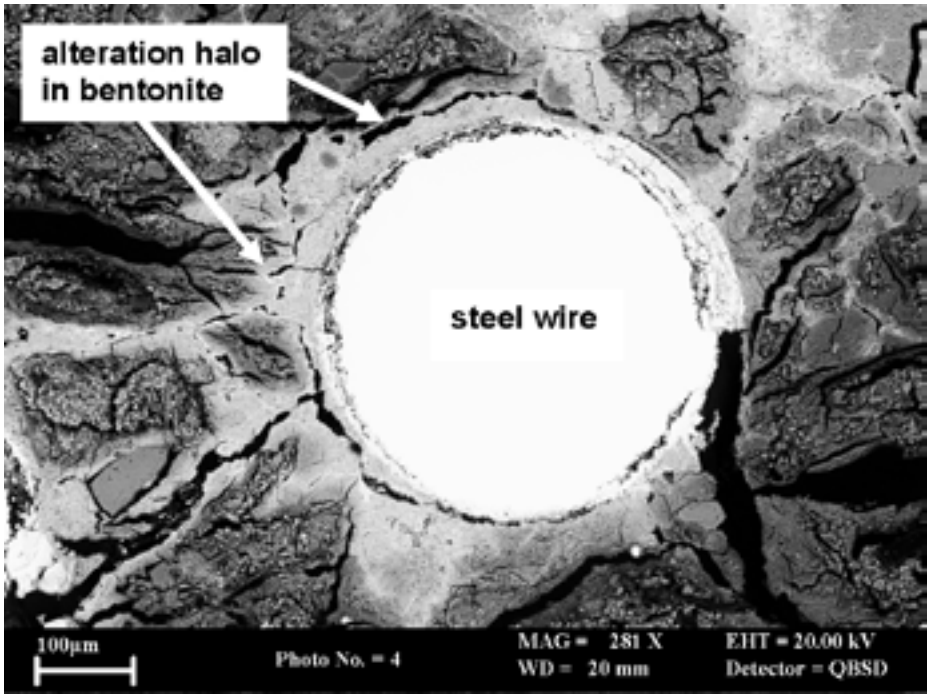

Figure 4-6. *BSEM photomicrograph of a corroded steel wire (white) in bentonite. The bentonite around the wire shows a halo of alteration (light grey) which also penetrates further into the bentonite clay matrix (darker grey) along microfractures radiating away from the wire. Disseminated angular grains of K-feldspar (mid grey) show no evidence of alteration. Experiment NFC12, subsample 12c.*

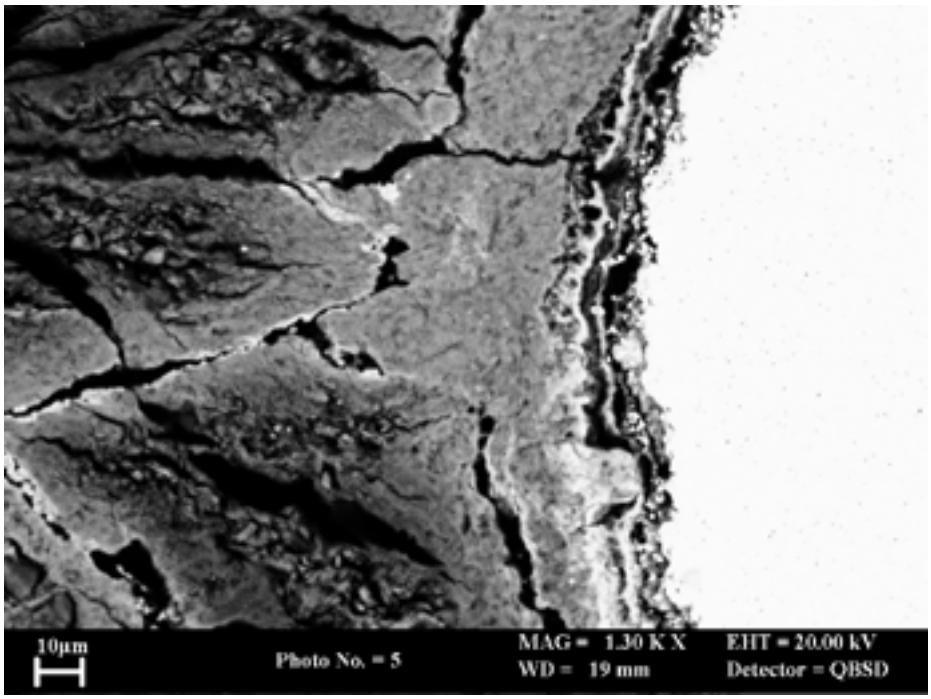

Figure 4-7. *BSEM photomicrograph showing detail of a corroded steel wire. The metal surface is surrounded by concentric bands of microporous iron oxide. Interconnected open microfractures in the clay matrix are lined by a fine layer of iron oxide or iron oxyhydroxide (bright). The fracture walls appear to have enhanced backscattered electron coefficient (i.e. appear brighter than the background clay) due to significant iron enhancement to a depth of up to 20 µm. Experiment NFC12, subsample 12c.*

Some of the microfracturing observed around the wires results from shrinkage due to the loss of water from the smectitic clay upon drying of the sample for section preparation and subsequent epoxy-resin impregnation. Such fractures are characterised by epoxy-resin impregnation but with no evidence of mineral alteration along the fracture walls. These shrinkage cracks usually cross-cut earlier microfractures that display mineralisation and wallrock alteration. The presence of Fe impregnation in the bentonite matrix of the fracture walls along earlier microfractures (e.g. Figure 4-7 and Figure 4-8) indicates that these features must have formed as a result of clay shrinkage during the course of the actual experiment and prior to any shrinkage during drying for sample preparation. Consequently, these must represent pathways for the migration of Fe away from the corroding metal surface.

X-ray elemental mapping reveals a more complex pattern of alteration around the corroded steel wires (Figure 4-9). In addition to being enriched in Fe, the alteration halo around the wire coincides with a reduction in Si and Al in the bentonite. Na and to some extent Mg, also show a depletion in the bentonite within the narrow alteration halo around the corroding metal. Part of this can probably be accounted for by the relative dilution of Si, Al, Na and Mg concentrations in the bentonite through the addition of Fe to the clay matrix from the corrosion of the steel. However, the Na depletion appears to be broader than that of the other elements. This may indicate that some Na has been displaced from the clay within the alteration zone. Fe is also shown to be very strongly concentrated within the clay matrix along fractures radiating away from the corroded steel. However, apart from linings along fracture walls and within the layer of corrosion products on the surface of the steel wire, little evidence could be found for the presence of an iron oxide phase within the Fe-enriched clay matrix, either as discrete particles or as pore-filling cement between the platy clay mineral particles (Figure 4-8). Within the limits of resolution of the BSEM technique (probably better than 0.1 µm) it would appear that the clay particles of the bentonite have become enriched in Fe within the alteration haloes.

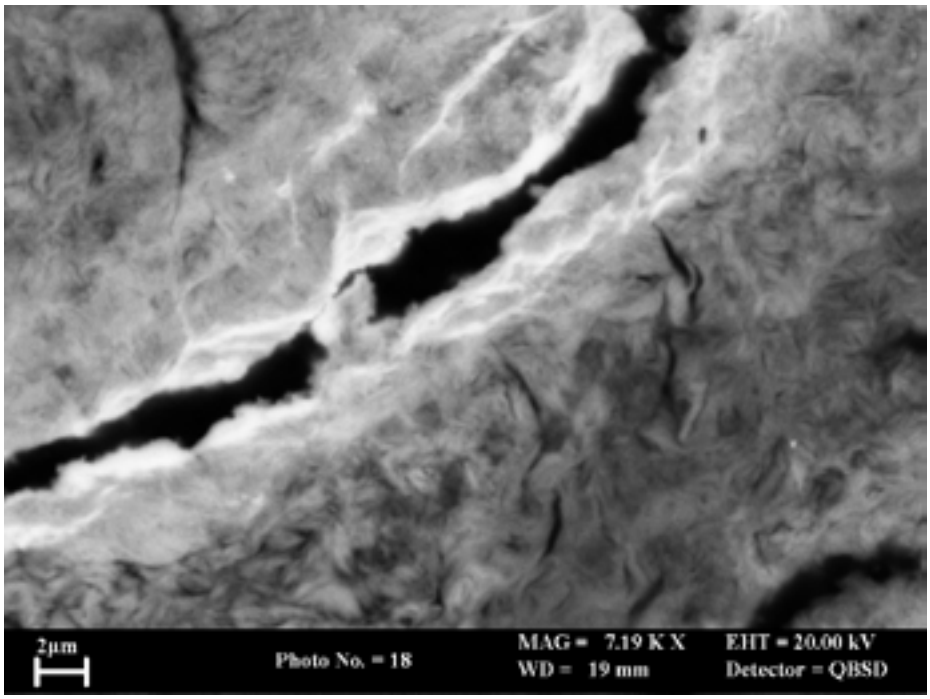

Figure 4-8. *BSEM photomicrograph showing fine detail of secondary iron oxide (bright) lining the wall of a microfracture in bentonite from close to a corroding steel wire. Iron oxide fills second-order microfractures in the walls of the primary fracture. The platy clay particles in the matrix in the bentonite fracture wall appear much brighter than background clay due to their enhancement in Fe but no discrete iron oxide phases could be differentiated in the altered clay matrix. Experiment NFC12, subsample 12c.*

Element distribution maps for Ca consistently displayed evidence for its concentration within the alteration halo (Figure 4-9). In most cases, Ca is seen to have concentrated within a narrow zone up to 20 µm wide in the bentonite resting immediately on top of the thin iron oxide corrosion product layer coating the surface of the metal (see also Figure 4-10). However, in some cases a series of narrow bands of Ca accumulation may be evident, each resting on the leading edge of diffusive fronts of enhanced Fe concentration within the altered clay matrix around the corroded wire, as seen in Figure 4-9. In addition, the microfractures radiating away from the steel wires may also show enhanced Ca along their surfaces. Carbon (C) concentrations coincide with the accumulation of Ca, suggesting that this reaction product may be a calcium carbonate phase, although it is often difficult to discriminate C in this Ca-rich alteration phase from the C present in the epoxy-resin used in making the polished thin sections. Detailed BSEM observation revealed that this Ca-rich phase occurs as clusters of fine acicular (needle-like) crystals (up to 10 µm long) precipitated on the walls of cavities within open microfractures around the margins of the corroded steel and in microfractures radiating away from the corroding wires. In addition, similar fine-grained acicular Ca-rich material is seen nucleated within, or replacing, the Fe-impregnated bentonite immediately adjacent to the iron oxide corrosion layer (Figure 4-11). It seems most likely that this neoformed Ca-phase corresponds to the aragonite that was identified from the altered bentonite by XRD (Section 4.2.2).

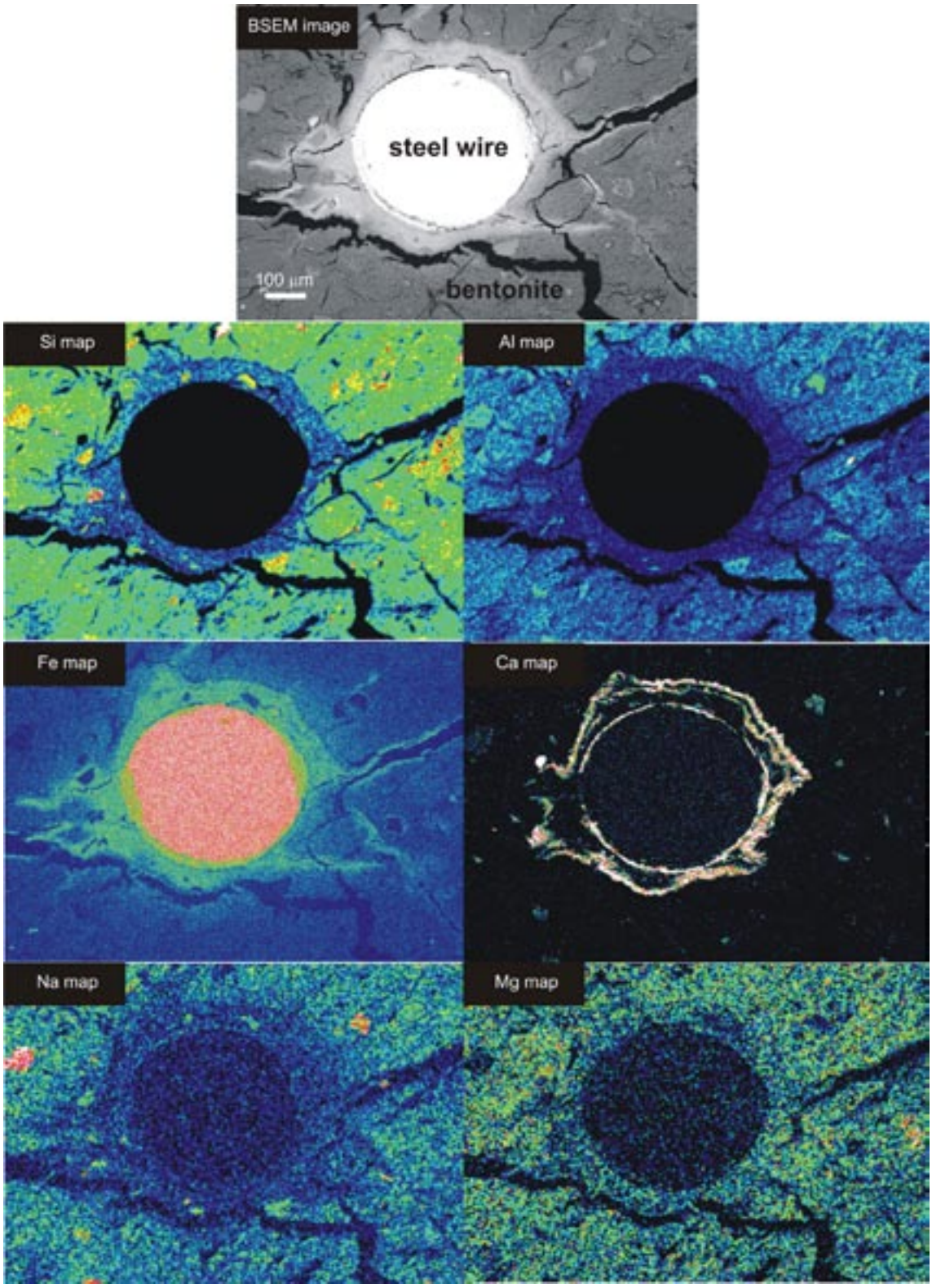

Figure 4-9. *EDXA elemental maps showing the distribution of Si, Al, Fe, Ca, Na and Mg around corroded steel wire within the field of view shown by the BSEM photo in Figure 4-6. Elements maps are thresholded and rainbow colour contoured to show high concentration as red to white colours and low concentration as black to blue colours. Experiment NFC12, subsample 12c.*

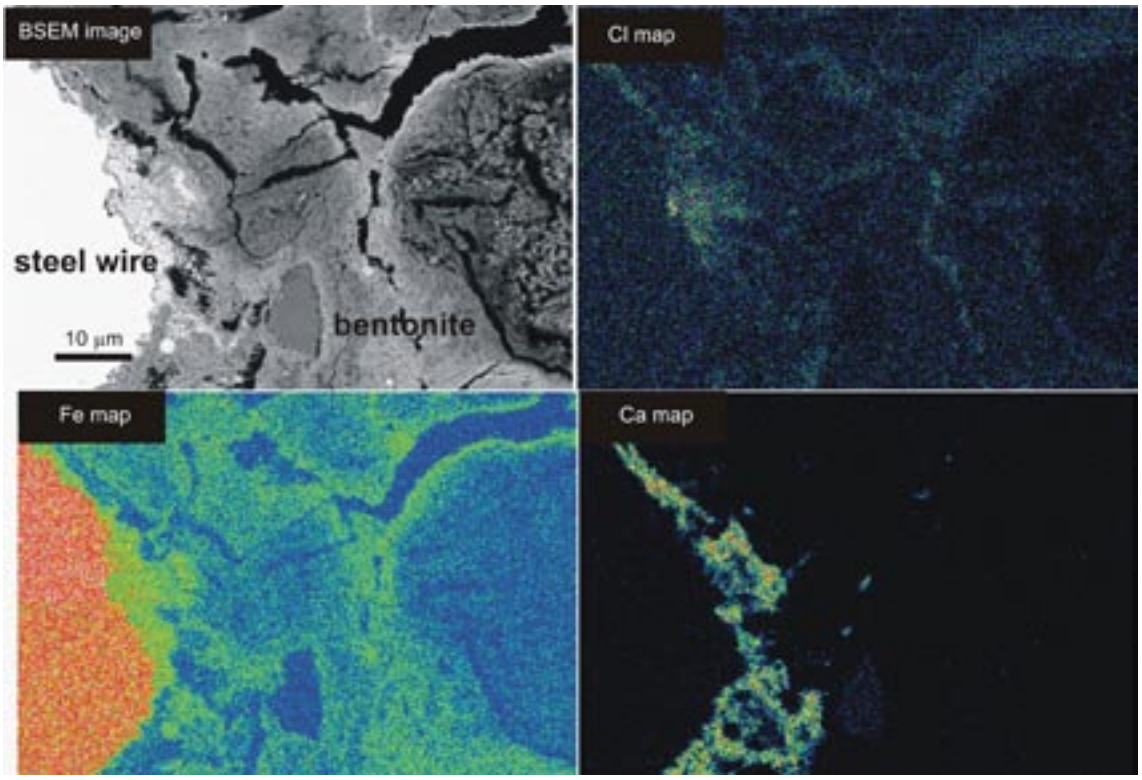

Figure 4-10. *High magnification EDXA elemental maps showing the detail of the distribution of Cl, Fe and Ca close to the surface of a corroded steel wire and along open microfractures in adjacent bentonite. Elements maps are thresholded and rainbow colour contoured to show high concentration as red to white colours and low concentration as black to blue colours. Experiment NFC12, subsample 12c.*

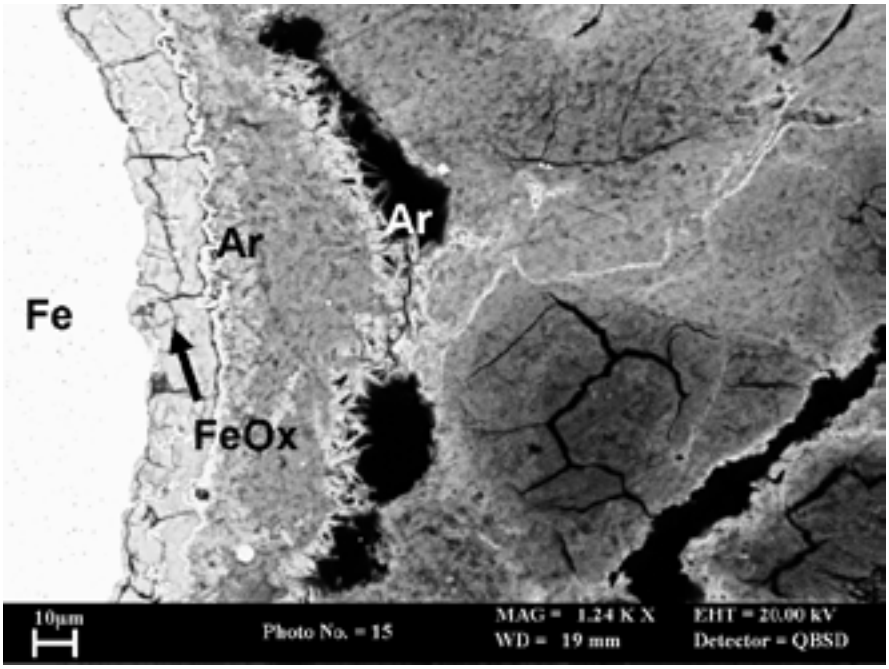

Figure 4-11. *BSEM photomicrograph showing aragonite needles (Ar) lining open shrinkage fractures within the alteration halo in bentonite around a corroded steel wire. The surface of the steel (Fe) is corroded and coated in gel-like iron oxide (FeOx). Clay matrix enriched in Fe appears brighter than unaltered smectitic clay Experiment NFC12, subsample 12c.*

Discrete angular grains of calcite, apatite were observed in the bentonite. These were originally present in the bentonite, and show no evidence of dissolution or alteration as a result of reaction during the experiment. Small spherical or framboidal aggregates of microcrystalline pyrite (FeS_2) were also identified. The pyrite appeared to be fresh and displayed no oxidation.

Occasionally, Cl concentrations were observed within the iron oxide corrosion layer on the surface of the steel (Figure 4-10). This may represent salt deposited from residual saline porewater but in most cases this is unlikely since it was not coincident with Na. The Cl appears to be closely associated with Fe as an Fe-Cl phase. However, it was too diffuse and fine grained to be characterised further by BSEM-EDXA.

X-ray elemental mapping showed no evidence for any alteration-related accumulation or depletion of Mn or P (e.g. Figure 4-9). In most cases, these elements were below the detection limit of the technique (likely to be of the order of 0.25–0.5 wt.% under the operating conditions used).

The shrinkage behaviour of the bentonite seen in thin section appears to have been affected by reaction with Fe from the corroding steel wires. Unaltered clay generally displays significantly greater shrinkage cracking (resulting from water loss during drying), than the Fe-enriched clay within the alteration haloes (Figure 4-11). This implies that the shrink-swell properties of the smectite (swelling clay) in the bentonite may have been reduced by reaction with Fe from the steel.

4.1.2 Experiment NFC16

General observations

Visual inspection of the cylinder of compacted bentonite recovered from Experiment NFC16 also indicated that significant alteration and reaction had occurred within the central region containing the dispersed steel wires, as evident from the very strong red-brown staining of the bentonite within this region (Figure 4-12). However, the extent of staining and apparent alteration was less than that observed in either Experiment NFC12 (see Section 4.1.1) or Experiment NFC17 (see Section 4.1.3). The staining of the bentonite extended no more than about 2–3 mm beyond the region containing the disseminated steel wires (Figure 4-13).

As in Experiment NFC12, the iron oxide staining permeated the bentonite along a ‘chicken-wire mesh-like’ network of interconnected hairline fractures (Figure 4-12), but with much less dense discolouration of the adjacent bentonite matrix (Figure 4-14).

Close examination of freshly broken fragments (after vacuum drying) showed that, as in Experiment NFC12, the surfaces of the steel wires from Experiment NFC16 were also coated with a black oxide corrosion product, surrounded by a halo of dark reddish-brown colouration of the adjacent bentonite that passed into a more diffuse and lighter orange to light reddish brown stain in the bentonite matrix beyond about 0.1–0.5 mm distance from the wire surface (Figure 4-3). Fragments of the dark brown to black oxide corrosion product also displayed ferromagnetic properties and could be attracted to a strong hand magnet. Again, it seems likely that this black oxide is probably similar to the magnetite alteration identified by XRD from the surfaces of corroded steel wires in Experiment NFC17 (see Section 4.2.2, Random orientation mount XRD).

There was little evidence on the surface of the bentonite cylinder of any ferruginous staining within the region of the bentonite containing the iron coupons (Figure 4-12). However, when freshly fractured surfaces through the bentonite-iron coupon interface were examined, the alteration characteristics were observed to be very similar to that seen in Experiment NFC12.

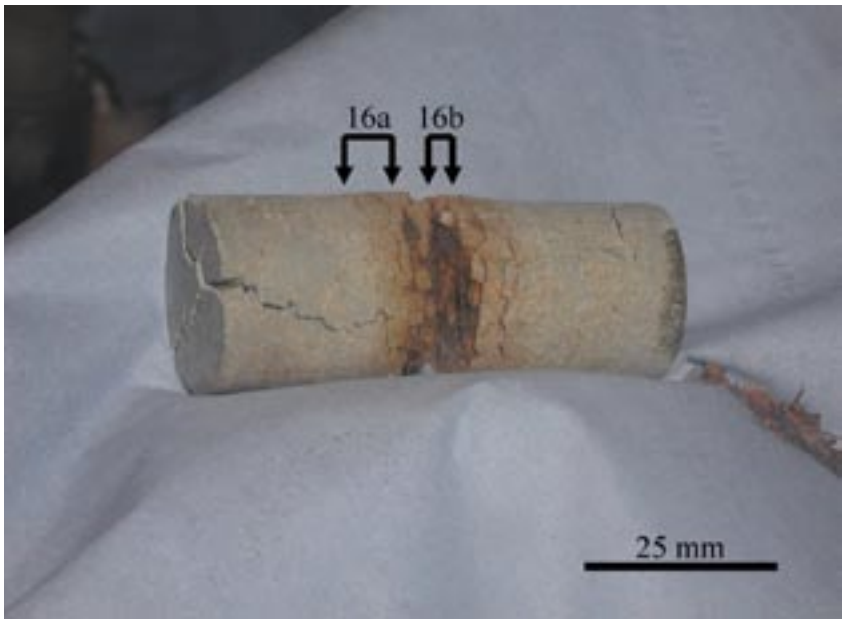

Figure 4-12. *Composite cylinder of compacted bentonite with steel wires and iron coupons recovered from Experiment NFC16 (photographed in nitrogen filled glove box). The central region containing the corroded steel wires is strongly stained by reddish brown iron oxide alteration, with staining along a network of fine fractures. Relatively fresh or unaltered grey-green bentonite remains at the end of the cylinder. The locations of subsamples taken for analysis are shown. [Photograph provided courtesy of Serco Assurance]*

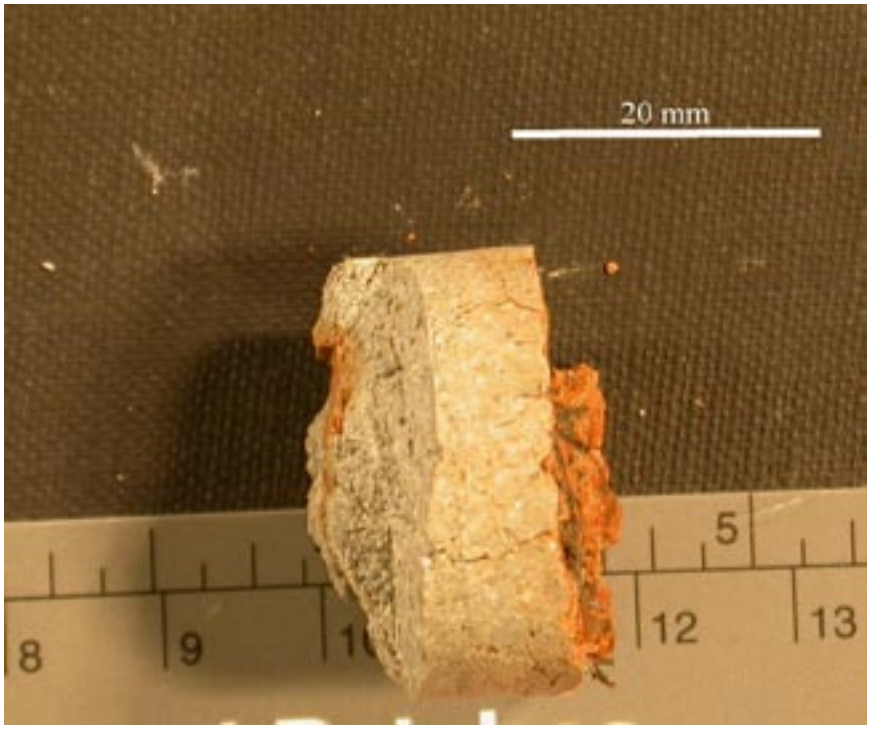

Figure 4-13. *Photograph of subsample 16a showing interface between bentonite and 'bentonite with steel wire' region (right), and interface between bentonite and iron coupon (left). Reddish brown staining permeates the matrix of the bentonite between the steel wires but there is only very limited penetration of 'iron staining' into the adjacent the wire-free bentonite. Experiment NFC16.*

Figure 4-14. *Photograph of subsample 16a showing the surface of the interface between bentonite and 'bentonite with steel wire' region. Reddish brown staining permeates the matrix of the bentonite between the steel wires but locally there are patches of iron-stain-free bentonite. The surfaces of the steel wires can be seen to be coated with a black oxide alteration product. Experiment NFC16.*

Detailed petrography

The petrographical characteristics of the interaction between the steel wire and the bentonite in Experiment NFC16 are broadly similar with those described above from Experiment NFC12. However, the extent of steel alteration and reaction with bentonite appears to be less well developed than either experiments NFC12 or NFC17. This is consistent with the general visual observations (Section 4.1.1, General observations) that also indicated much reduced degree of iron staining of the compacted bentonite matrix in this experiment.

Very narrow alteration haloes, comprising Fe-enriched clay matrix, are seen in the bentonite adjacent to corroded steel wires (Figure 4-15). They are typically of the order of 10–50 µm wide compared to the much thicker alteration zones up to 250 µm wide that are seen around steel wire in experiments NFC12 and NFC17. However, the alteration assemblage is very similar. A thin layer of very fine or gel-like iron oxide (or oxyhydroxide) corrosion product was formed directly on the pitted steel surface (Figure 4-16). XRD analyses (see Section 4.2.2, Random orientation mount XRD) tentatively suggest that this may be åkaganeite (β-FeO[OH, Cl]). In turn, this is surrounded by a narrow zone of bentonite, which has been significantly enriched in Fe. The Fe enrichment of the clay matrix locally permeates further into the bentonite along hairline microcracks. Semi-quantitative observations indicate that the altered clay contains several weight percent of Fe (although the actual concentrations of Fe were not determined).

Detailed BSEM observations found no evidence for discrete iron oxide disseminated within the altered bentonite, and it appears from these observations that the clay particles themselves have become enriched in Fe.

X-ray elemental mapping showed that an enhanced but diffuse concentration of Fe sometimes permeated the bentonite beyond the alteration haloes evident from BSEM observation alone (Figure 4-17). Often the distribution of Fe appeared to be somewhat irregular, and in some cases X-ray mapping suggested enhancement of Fe in the clay matrix may locally penetrate up to 200 µm from the corroded metal surface.

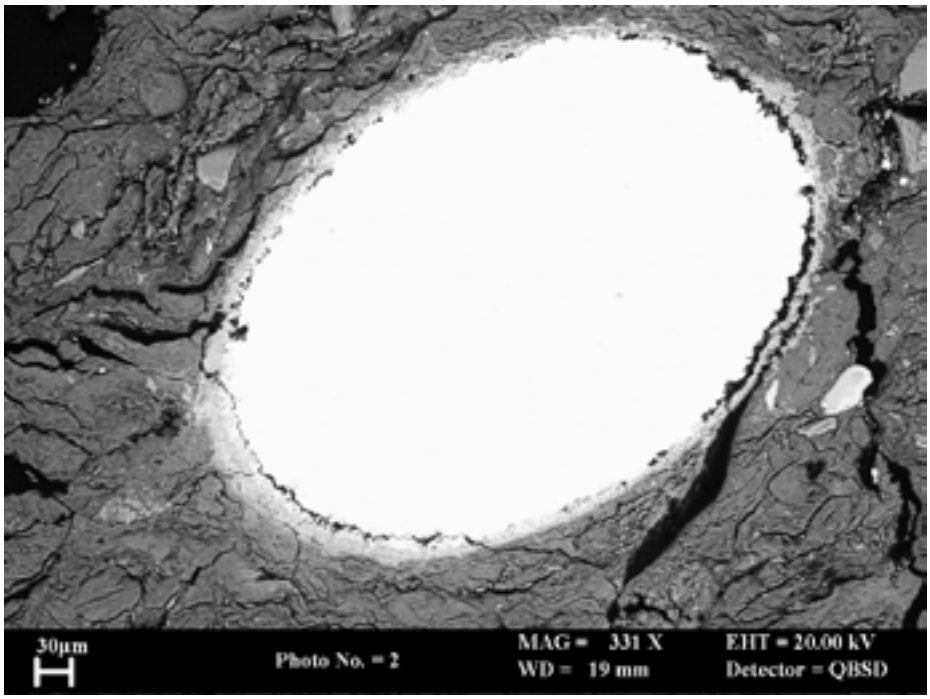

Figure 4-15. *BSEM photomicrograph showing reacted steel wire surrounded by a thin alteration halo comprising iron oxide, aragonite and Fe-enriched altered bentonite. Experiment NFC16, subsample 16a.*

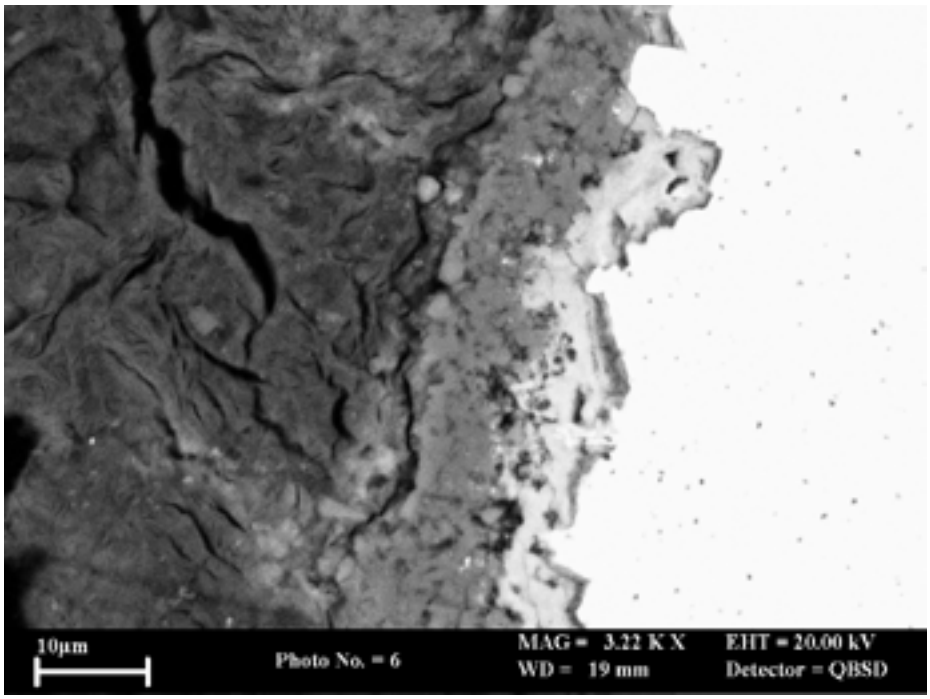

Figure 4-16. *BSEM photomicrograph showing detail of the thin alteration halo around a corroded steel wire. The steel wire (white) is pitted and coated with a thin layer of iron oxide corrosion product (bright). A thin coating of aragonite (mid grey) rests on the iron oxide at the interface with the bentonite (dark grey). Wispy brighter areas within the bentonite matrix are enhanced with Fe along microfractures. Experiment NFC16, subsample 16a.*

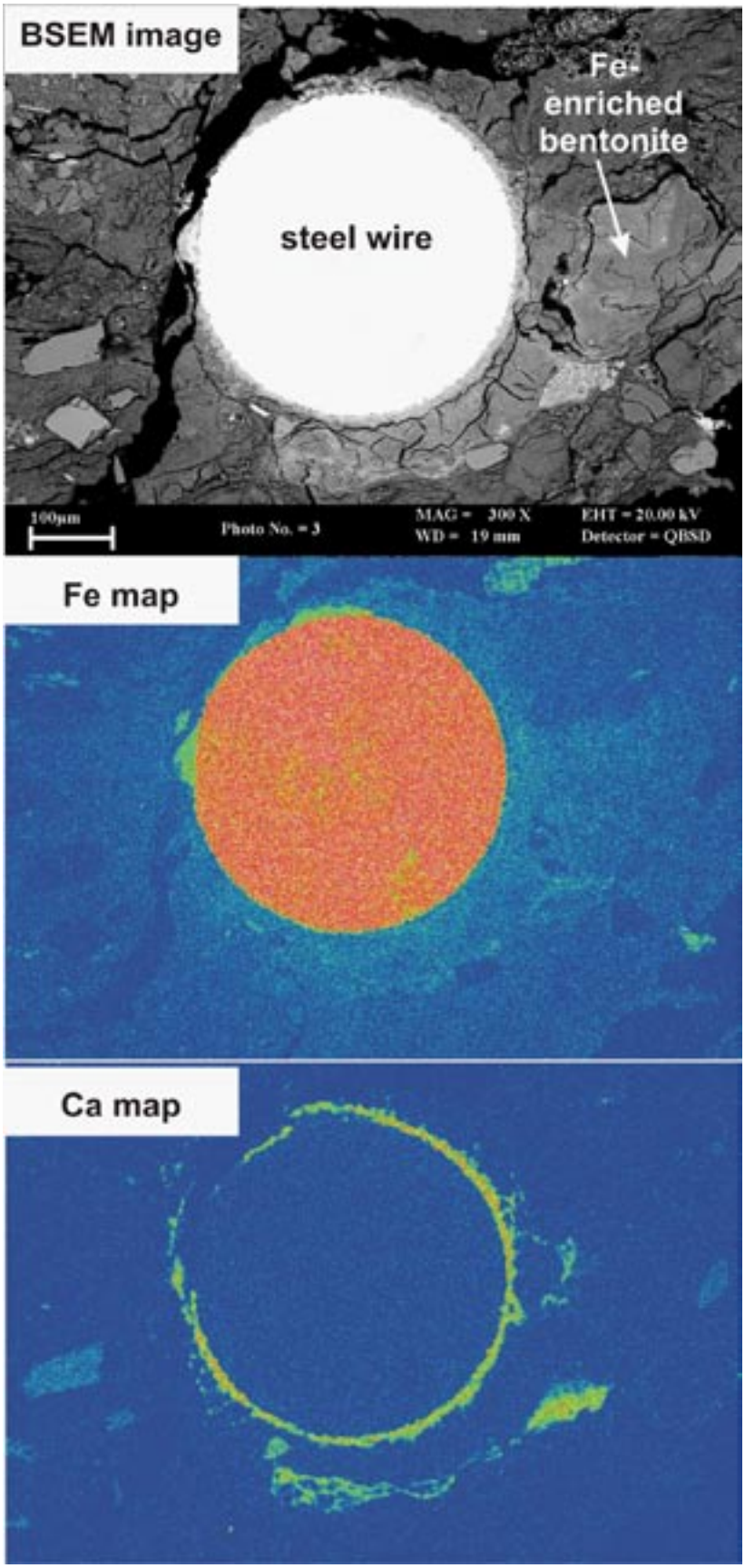

Figure 4-17. *EDXA elemental maps showing the distribution of Fe and Ca around a corroded steel wire and along open microfractures in adjacent bentonite. Elements maps are thresholded and rainbow colour contoured to show high concentration as red to white colours and low concentration as blue colours. Experiment NFC16, subsample 16a.*

Ca is also shown by X-ray element mapping to be markedly concentrated at the interface between the corroded metal and the enclosing clay matrix (Figure 4-17). Ca may also be concentrated at the leading edges of Fe diffusion fronts within the altered bentonite haloes (as seen in the lower part of image area in Figure 4-17). Detailed BSEM observations indicate that this corresponds to a thin band of calcium carbonate, 10–15 μm thick, which most probably accounts for the aragonite identified by XRD from the altered bentonite (Section 4.2.2).

Broadly similar features were observed to that described previously from Experiment NFC12, in the distribution of Si and Al around the steel wires within the altered bentonite. However, no significant modification in the distribution of Na, Mg and Cl could be detected. K, P and S were only found where minor to accessory grains of K-feldspar, apatite or pyrite were present.

Discrete angular grains of calcite and apatite were observed in the bentonite. These were originally present in the bentonite, and show no evidence of dissolution or alteration as a result of reaction during the experiment. Small spherical or framboidal aggregates of microcrystalline pyrite (FeS_2) were also identified. The pyrite appeared to be fresh and displayed no oxidation.

4.1.3 Experiment NFC 17

General observations

Visual inspection of the cylinder of compacted bentonite recovered from Experiment NFC17 indicated that significant alteration and reaction had occurred within the central region containing the dispersed steel wires, as evident from the very strong red-brown staining of the bentonite within this region (Figure 4-18). The pattern of discolouration, with permeation of iron oxide along a 'chicken wire mesh-like' network of interconnected hairline fractures within this central region and extensive penetration into the adjacent bentonite matrix, was similar to that observed in Experiment NFC12.

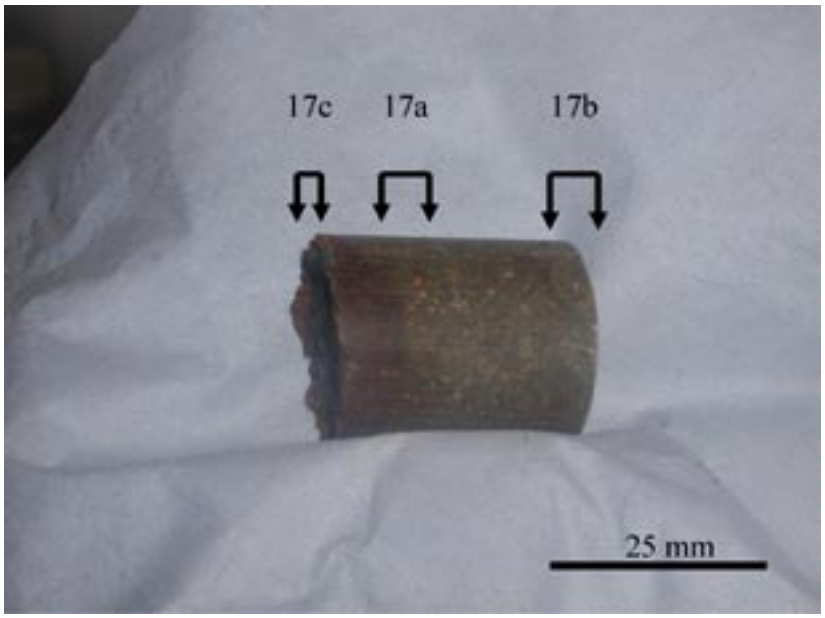

Figure 4-18. *Composite cylinder of compacted bentonite with steel wires and iron coupons recovered after experimentation from Experiment NFC17 (photographed in nitrogen filled glove box). The central region containing the corroded steel wires is strongly stained by reddish brown iron oxide alteration. Relatively fresh or unaltered grey-green bentonite remains at the end of the cylinder. The locations of subsamples taken for analysis are shown. [Photograph provided courtesy of Serco Assurance]*

The region of the bentonite containing the iron coupons also displayed a slight ferruginous discolouration of the grey green bentonite (as, for example, seen just to the left of the region indicated by sample 17b in Figure 4-18).

As with experiment NFC12 and NFC16, close examination of freshly broken fragments (after vacuum drying) showed that the surfaces of the steel wires from Experiment NFC17 were also coated with a black oxide corrosion product, surrounded by a matrix of dark reddish-brown bentonite (Figure 4-19). Fragments of this dark brown to black oxide corrosion product scraped from the wire surfaces were found to be attracted to a strong hand magnet and was identified by XRD to contain magnetite (see Section 4.2.2, Random orientation mount XRD).

Detailed petrography

BSEM petrographical examination revealed that the steel wires in Experiment NFC17 displayed significant corrosion, and that the Fe released from the steel had interacted with the adjacent bentonite clay matrix (Figure 4-20). The degree of alteration appeared to be similar to, or slightly more intense than, that seen in Experiment NFC12, with alteration haloes around the corroded steel wires reaching up to 300 µm wide. As in the other two experiments, the alteration and iron enrichment of the clay locally penetrated further into the matrix along hairline micro-fractures radiating out from the wires. Close examination also showed that iron enrichment and impregnation had also occurred along the boundaries of subangular to subrounded sand-sized ‘domains’ that probably represent the original granular bentonite clast fragments of the bentonite material used in the manufacture of the compacted bentonite-steel wire-iron coupon composites, prior to hydration (Figure 4-20).

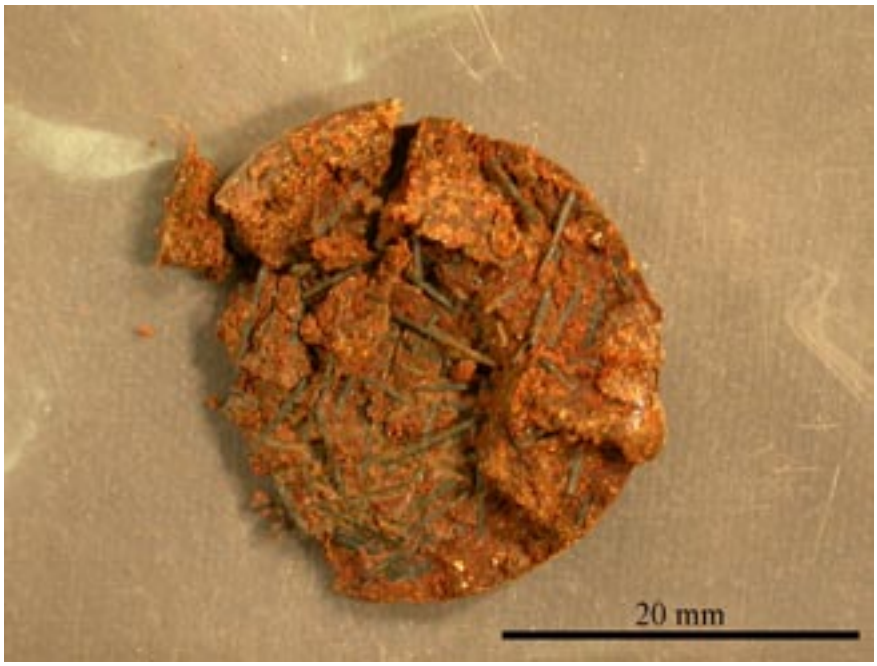

Figure 4-19. *Photograph of bentonite with corroded steel wires from the centre of the steel wire-bentonite zone. The steel wires are covered by a surface film of black iron oxide. The bentonite matrix between the wires is heavily stained an orange to reddish brown colour. Experiment NFC17.*

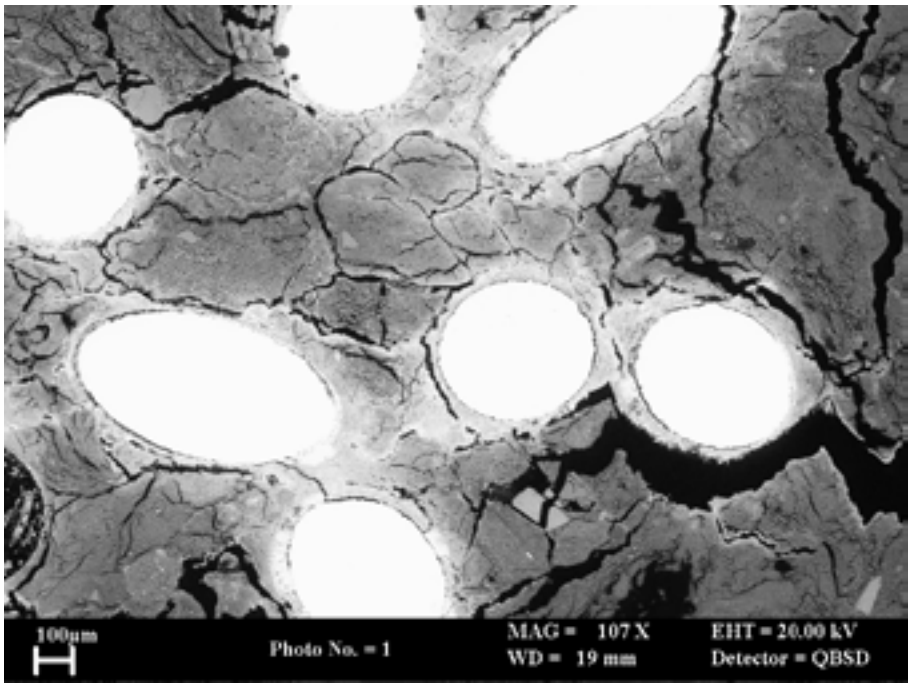

Figure 4-20. *BSEM photomicrograph showing extensive alteration halos around corroded steel wires (white) in bentonite matrix. The altered clay matrix appears brighter than the background unaltered clay due to enrichment with Fe from the corroded metal. Boundaries of the original bentonite clasts are discernable as a result of Fe-enrichment of the clay matrix adjacent to the clast surfaces. Experiment NFC17, subsample 17a.*

Detailed BSEM observations and X-ray elemental mapping of the sample (Figure 4-21) showed similar patterns of alteration to those observed in experiments NFC12 and NFC16. The surfaces of the steel wires are pitted and corroded, with a fine layer of fine grained iron oxide or oxy-hydroxide corrosion product that has formed directly on the corroded steel wire surface. This oxide layer appears to be better developed than on the steel wires in Experiment NFC12, locally reaching up to 50 µm in thickness (Figure 4-21). XRD analyses (see Section 4.2.2, Random orientation mount XRD) tentatively suggest that this may be åkaganeite (β-FeO[OH, Cl]). Thin layers of iron oxide precipitate also coat the walls of networks of hairline fractures in the clay matrix, radiating away from the steel wires. These fractures may be open, with apertures from 1 µm up to 40 µm. Although X-ray mapping shows significant Fe-enrichment of the bentonite matrix between the corroding wires, detailed BSEM observation found no evidence of discrete iron oxide within the clay matrix, and the Fe appears to be present (within the resolution limits of the technique) within the clay mineral particles themselves.

As in the two experiments described previously, X-ray elemental maps show that Ca is concentrated within the bentonite around the corroded steel (Figure 4-21). The Ca enrichment occurs on top of the iron oxide fringe coating the steel wires. It is also concentrated on top of the iron-enriched bentonite forming the walls of hairline fractures in the altered bentonite. Close examination by BSEM-EDXA shows that the Ca corresponds to the development of a layer of microgranular calcium carbonate which nucleated within iron-rich clay matrix immediately adjacent to microcavities (Figure 4-22). The cavities are then lined by needles of iron oxide or oxyhydroxide, with individual crystals up to 20 µm long and forming alteration fringes that are locally up to 30 µm thick. Needles of aragonite were also seen, and their morphology and distribution is consistent with the identification of aragonite by XRD in bentonite adjacent to the steel wires (Section 4.2.2).

Other element distributions are similar to those described from Experiment NFC12.

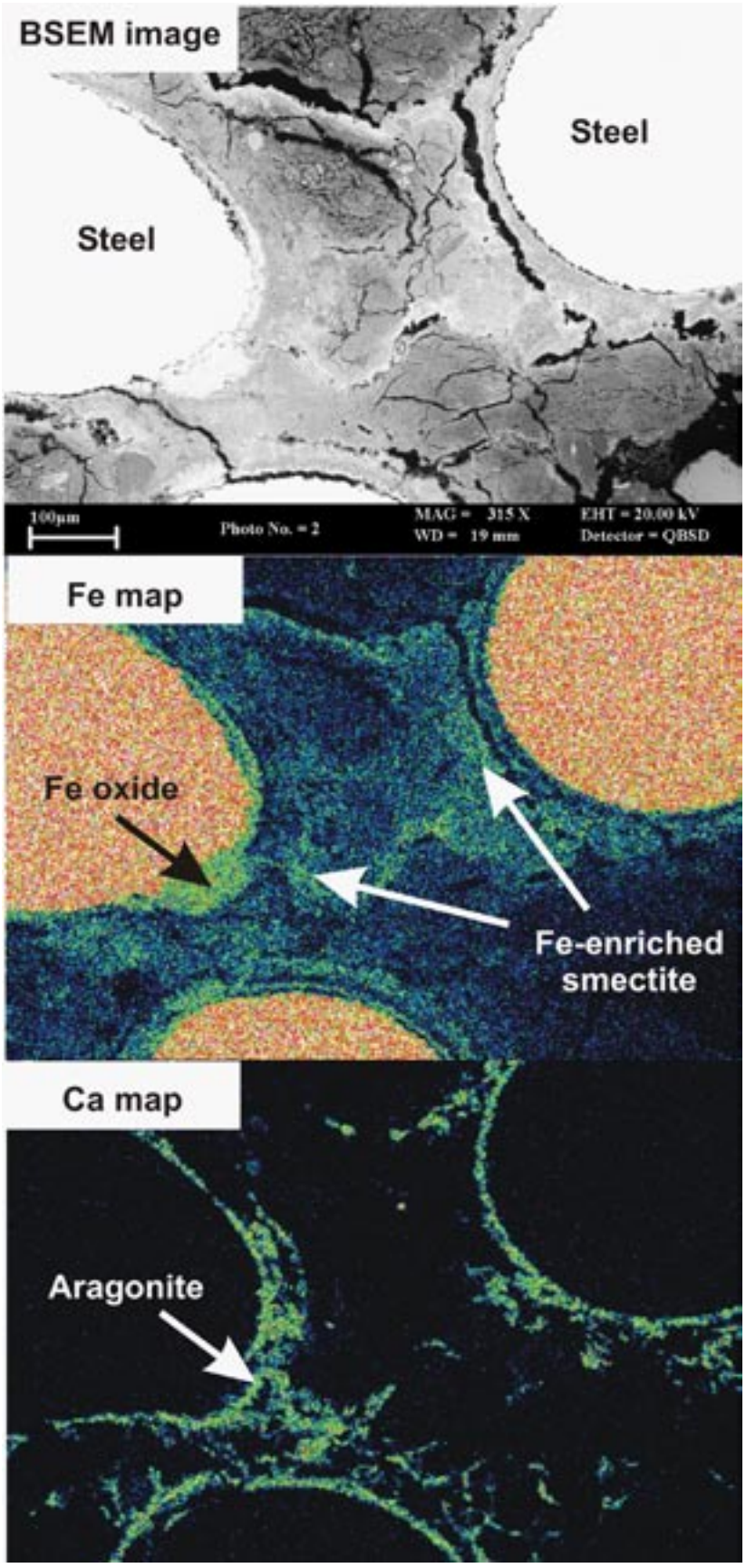

Figure 4-21. *EDXA elemental maps showing the distribution of Fe and Ca around corroded steel wires and along open microfractures in adjacent bentonite matrix. Elements maps are thresholded and rainbow colour contoured to show high concentration as red to white colours and low concentration as black to blue colours. Experiment NFC17, subsample 17a.*

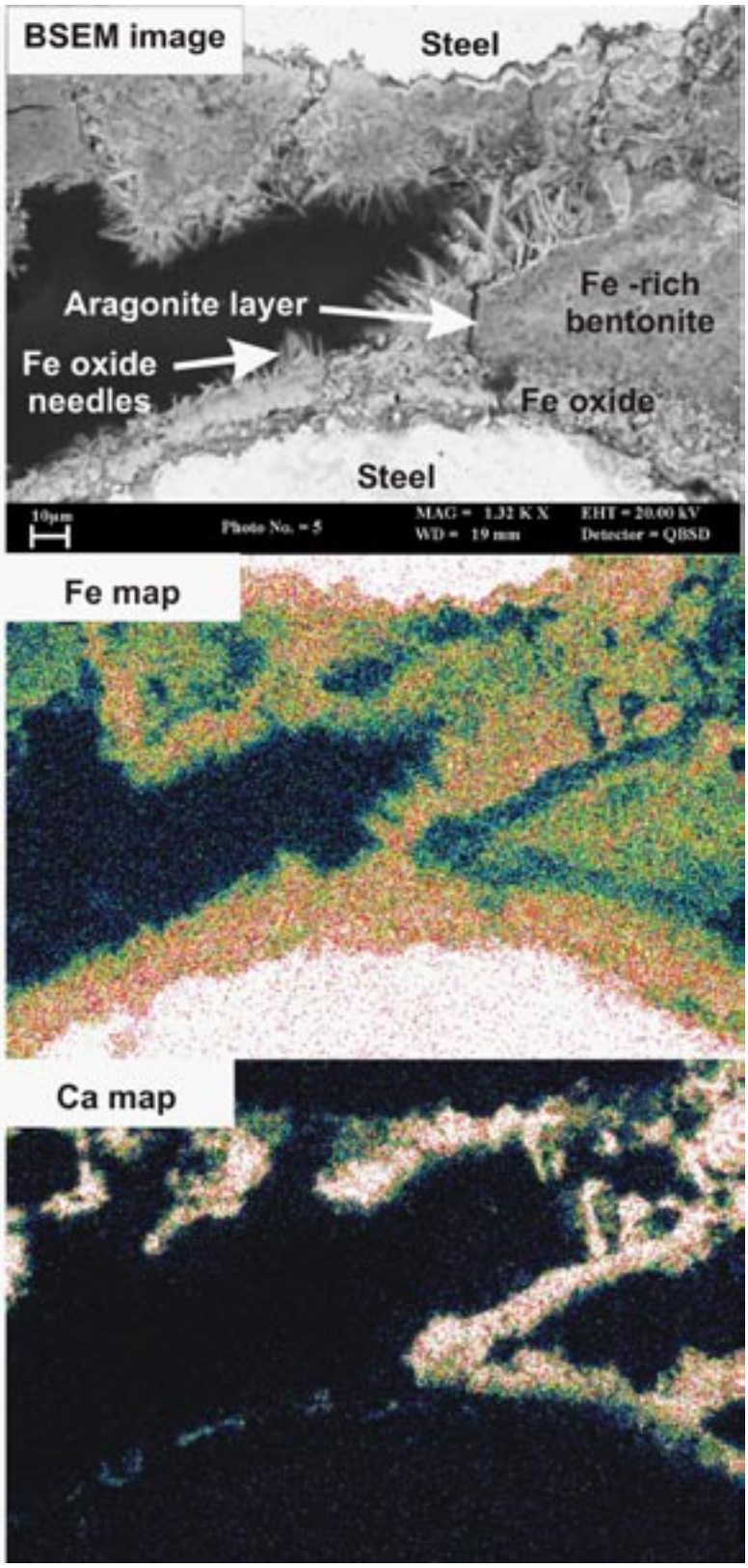

Figure 4-22. *High magnification EDXA elemental maps showing the detailed distribution of Fe and Ca around a corroded steel wire and along open microfractures in the interstitial bentonite matrix. The maps show that a Ca-rich reaction product corresponding to a layer of aragonite on top of Fe-enriched bentonite, and coated by needles of iron oxide or oxyhydroxide lining microcavities in the bentonite adjacent to corroding steel wire. Element maps are thresholded and rainbow colour contoured to show high concentration as red to white colours and low concentration as blue colours. Experiment NFC17, subsample 17a.*

Discrete angular grains of calcite and apatite were observed in the bentonite. These were originally present in the bentonite, and show no evidence of dissolution or alteration as a result of reaction during the experiment. Small spherical or framboidal aggregates of microcrystalline pyrite (FeS_2) were also identified. The pyrite appeared to be fresh and displayed no oxidation.

The unaltered background clay generally displays significantly greater shrinkage cracking (resulting from water loss during drying) than the Fe-enriched clay within the alteration haloes adjacent to the corroded steel wires. This implies that the shrink-swell properties of the smectite (swelling clay) in the bentonite may have been reduced or inhibited as a result reaction with Fe from the steel.

4.2 X-ray diffraction analysis

The results of XRD analyses are summarised in Table 4-1 and Table 4-2.

4.2.1 Unaltered background bentonite

Random orientation mount XRD

Random orientation XRD analyses indicate that the 'unaltered', grey-green bentonite from Serco Experiments NFC12, NFC16 and NFC17 (Table 4-1) is predominantly composed of a smectite-group mineral together with minor-to-trace amounts of quartz, halite, cristobalite, feldspar (albite and K-feldspar) and pyrite, and in some cases traces of undifferentiated mica species (the term 'mica', as used here, possibly including muscovite, biotite, illite, illite/smectite etc), calcite, gypsum and goethite (Figure 4-23).

A mean d_{060} dimension of 1.4965 Å (range of values 1.4957 to 1.4972 Å) for the 'unaltered' grey-green bentonite subsamples indicates that the smectite-group mineral can be classified as dioctahedral and most likely is a montmorillonite species.

The montmorillonite in the 'unaltered' grey-green bentonite subsamples displays a mean d_{001} spacing of c.12.74 Å (range of values 12.72 to 12.77 Å) suggesting that monovalent (i.e. Na and/or K) cations dominate the smectite interlayer cations. Measurements of the width of the montmorillonite d_{001} peak, which provides an indication of the crystallite-size distribution of the phase, produce a mean FWHM (Full Width at Half Maximum) of 0.59 ± 0.03 $\Delta°2\theta$ for the 'unaltered' bentonite samples.

Oriented mount XRD

Oriented mount XRD analyses (Table 4-2) confirm that the clay mineral assemblages of the 'unaltered' bentonite are dominated by montmorillonite with small quantities of 'mica' (the term 'mica', as used here, includes illite, which is not differentiated by this analysis). As well as the non-clay minerals identified by random orientation XRD (see Section 4.2.1, Random orientation mount XRD), a low intensity peak at 8.92 Å in the air-dry traces of all three 'unaltered' bentonite samples additionally suggest the presence of small quantities of a zeolite-group mineral, probably heulandite.

Montmorillonite was identified by an air-dry d_{001} spacing of c.11.5 Å (range of values 11.2 to 11.6 Å) which expands to a similarly typical c.17 Å on glycol-solvation and collapses under heating to 550°C for 2 hours to an 'illite-like' 9.6 Å d_{001} spacing. The montmorillonite d_{001} FWHM has a range of 1.46 to 1.64 $\Delta°2\theta$ and a mean value of 1.52 $\Delta°2\theta$.

The montmorillonite d_{001} intensities can also be used to gain information on Fe substitution by measuring the scattering from the clay mineral octahedral sheet. The intensity ratio of the d_{002} to the d_{003} increases as the total number of electrons in the octahedral sheet increases. d_{002}/d_{003} values for the 'unaltered' bentonite subsamples range from 0.99 to 1.25 (mean 1.11).

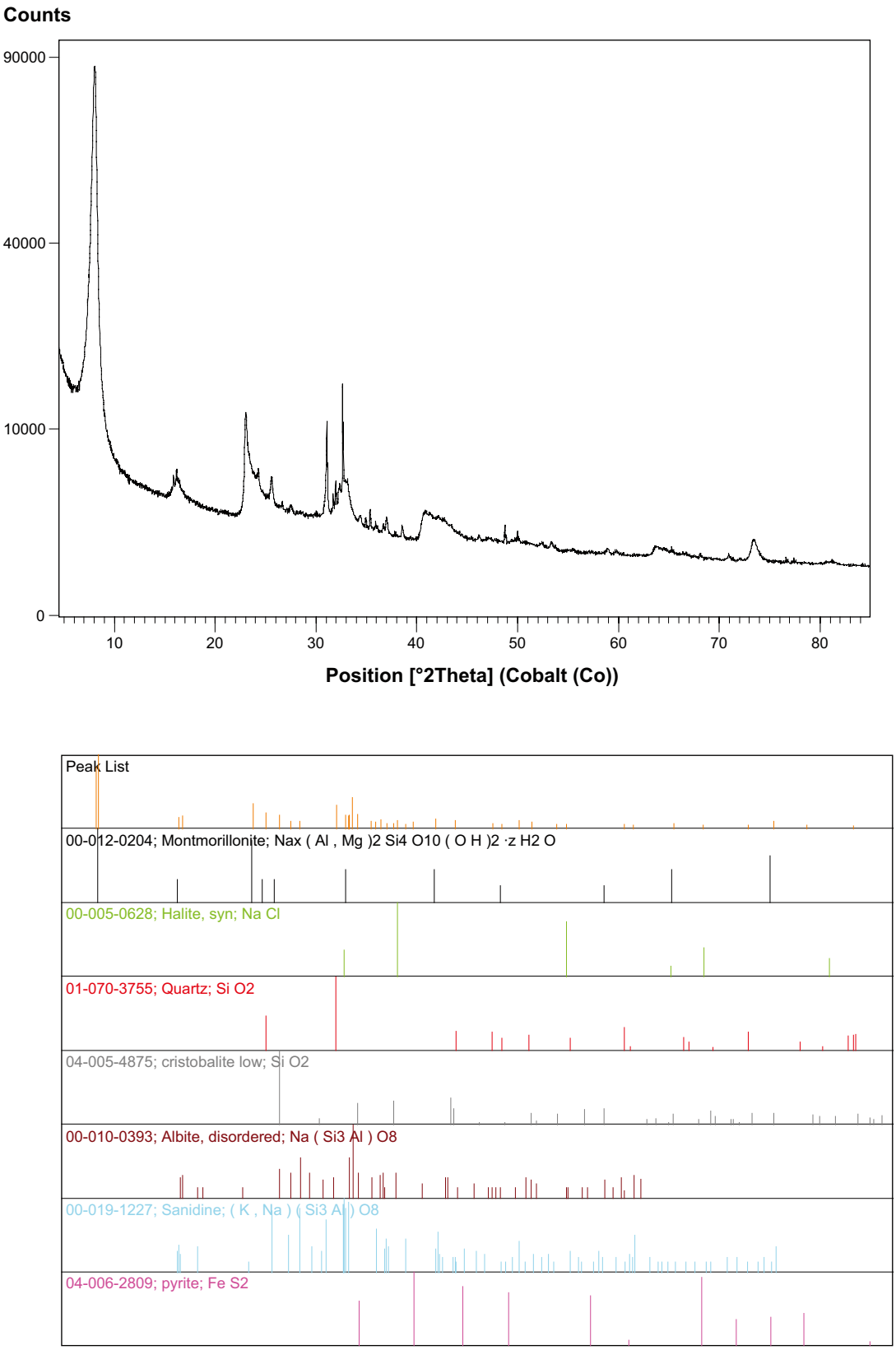

Figure 4-23. *Random powder mount XRD trace for 'unaltered' bentonite material (upper figure) compared to stick patterns for extracted peak information and ICDD standard patterns for the identified mineral phases (lower figure), Experiment NFC 12, sample 12a.*

'Mica' was identified by its characteristic air-dry d_{001} spacing of c.10.0 Å which remains invariant after glycol-solvation and heating. A broad, low intensity superlattice peak at c.21.8 Å on the air-dry XRD trace which expands to c.31.4 Å on glycolation could not be definitively identified but may suggest the presence of trace amounts of an interlayered smectite-bearing phase.

4.2.2 Altered bentonite adjacent to corroded steel wire and iron coupon

Random orientation mount XRD

Random orientation XRD analyses of the pervasively-stained bentonite in contact with the corroded steel wires indicate that it has a generally similar mineralogy to the 'unaltered' bentonite (Table 4-1). It is predominantly composed of a smectite-group mineral together with minor-to-trace amounts of quartz, halite, cristobalite, feldspar (albite and K-feldspar), and an undifferentiated mica species (which possibly includes muscovite, biotite, illite, illite/smectite etc), sometimes with traces of pyrite and a zeolite-group mineral (probably heulandite). Although undetected in the 'unaltered background' grey-green bentonite, significant aragonite was also detected in the altered iron-stained bentonite immediately adjacent to corroding steel wires from Experiment NFC16, sample 16b. Further random orientation XRD analyses of the bentonite/corrosion products removed from the surface of the corroded wires from Experiments NFC16 and NFC17 similarly detected the presence of aragonite along with the more typical bentonite mineral assemblage (Figure 4-24). Magnetite was also detected in the surface of the corroded wires from Experiment NFC17, sample 17c. A low intensity peak at c.7.4 Å detected in all the subsamples taken from the wire surfaces but not observed in the XRD traces from other subsamples, was tentatively attributed to the presence of the poorly crystalline iron oxyhydroxide phase, åkaganeite [FeO(OH,Cl)] (Figure 4-24).

A mean d_{060} dimension of 1.4965 Å (range of values 1.4961 to 1.4969 Å) for the altered bentonite subsamples indicates that the smectite-group mineral is dioctahedral and most likely to be a montmorillonite species (Figure 4-25).

The montmorillonite in the altered bentonite subsamples displays a mean d_{001} spacing of c.12.82 Å (range of values 12.76 to 12.88 Å) and a mean FWHM of 0.64 Δ°2θ (range 0.59 to 0.73 Δ°2θ). This compares with a mean d_{001} spacing of c.12.88 Å (range of values 12.86 and 12.89 Å) and a mean FWHM of 0.89 Δ°2θ (range 0.86 and 0.91 Δ°2θ) for the subsamples taken from the surface of the wires (Figure 4-26).

Oriented mount XRD

Oriented mount XRD analyses (Table 4-2) confirm that the clay mineral assemblages of the 'unaltered' bentonite are dominated by montmorillonite with small quantities of 'mica'. As well as the non-clay minerals identified by random orientation XRD (see Section 4.2.2, Random orientation mount XRD), a low intensity peak at 8.92 Å in the traces of most of the altered bentonite samples additionally suggest the presence of small quantities of a zeolite-group mineral, probably heulandite.

Montmorillonite was identified by an air-dry d_{001} spacing of c.11.7 Å (range of values 11.4 to 11.9 Å) which expands to a similarly typical c.17 Å on glycol-solvation and collapses under heating to 550°C for 2 hours to an 'illite-like' 9.6 Å d_{001} spacing. The montmorillonite d_{001} FWHM has a range of 1.43 to 1.68 Δ°2θ and a mean value of 1.55 Δ°2θ (Figure 4-27).

The montmorillonite d_{001} intensities can also be used to gain information on Fe substitution by measuring the scattering from the clay mineral octahedral sheet. The intensity ratio of the d_{002} to the d_{003} increases as the total number of electrons in the octahedral sheet increases. d_{002}/d_{003} values for the altered bentonite subsamples range from 1.04 to 1.48 (mean 1.17).

'Mica' was again identified by its characteristic air-dry d_{001} spacing of c.10.0 Å which remains invariant after glycol-solvation and heating. The very low intensity, superlattice peak noted in the 'unaltered' bentonite samples is also apparent in the altered samples, particularly at c.31.4 Å on the glycol-solvated trace.

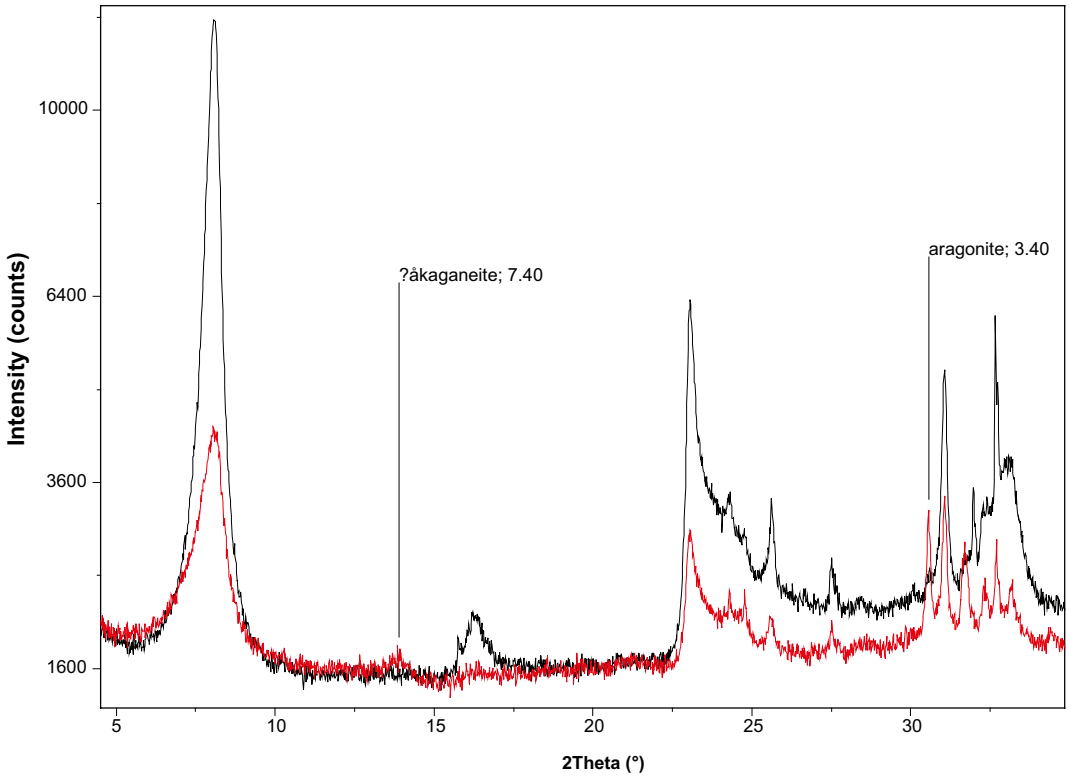

Figure 4-24. *Section of random powder mount XRD traces for altered bentonite material (black trace) and material removed from the surface of the corroding wire (red trace). Diagnostic peak positions for the alteration products for possible åkaganeite and aragonite are shown, Experiment NFC 17, sample 17a.*

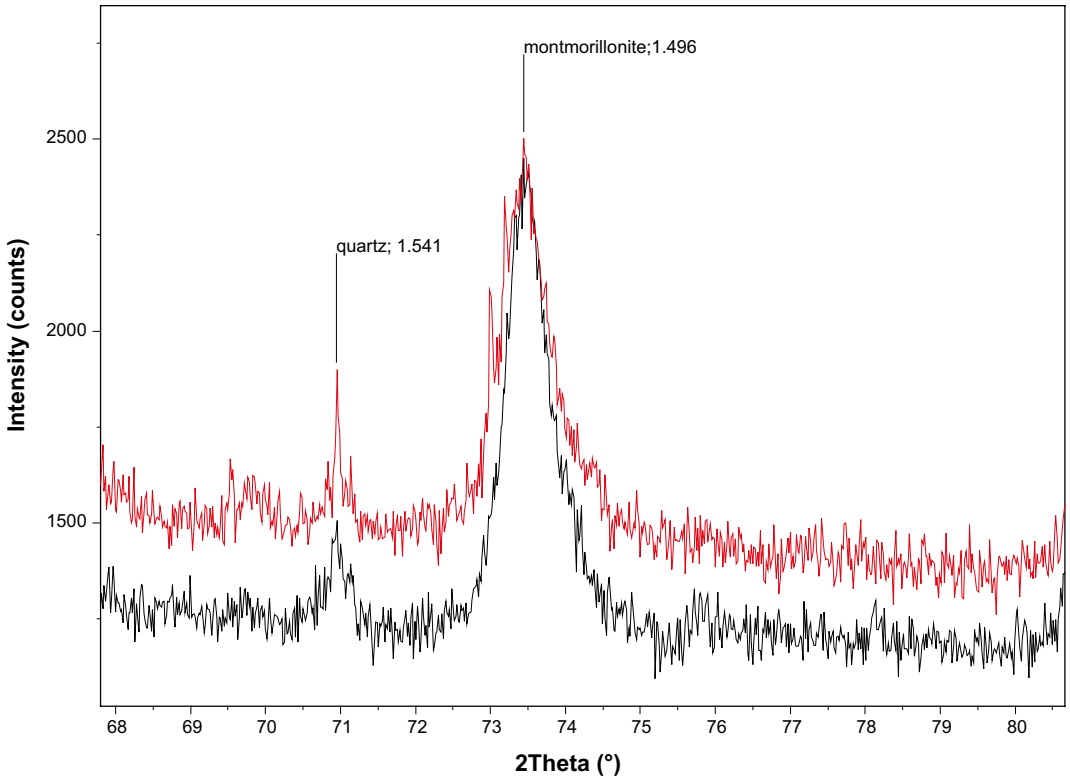

Figure 4-25. *High angle section of random powder mount XRD traces for 'unaltered' material (black trace) and altered material (red trace) to illustrate a lack of change in the montmorillonite* $\mathbf{d}_{060}$ *spacing, Experiment NFC 12, sample 12b.*

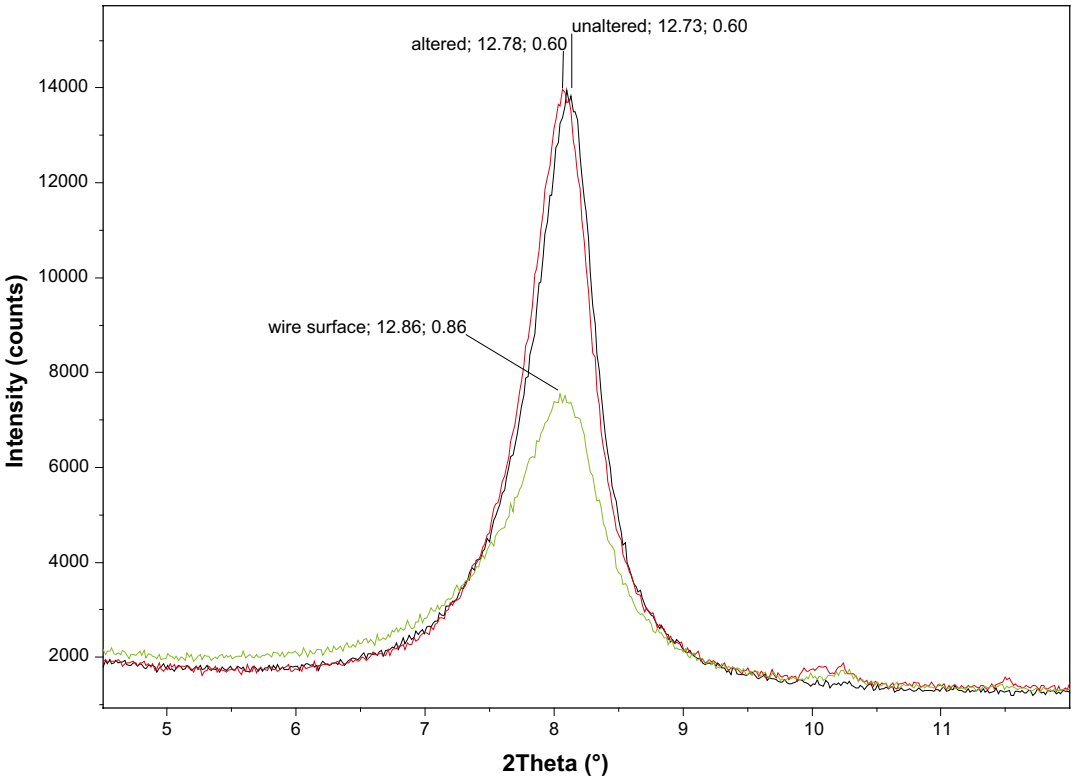

Figure 4-26. *Low angle section of random mount XRD traces to illustrate increase in spacing (Å) and FWHM for the montmorillonite* $\mathbf{d}_{001}$ *peak in altered material (red trace) and wire surface material (green trace) compared to the 'unaltered' material (black trace), Experiment NFC 16, sample 16a.*

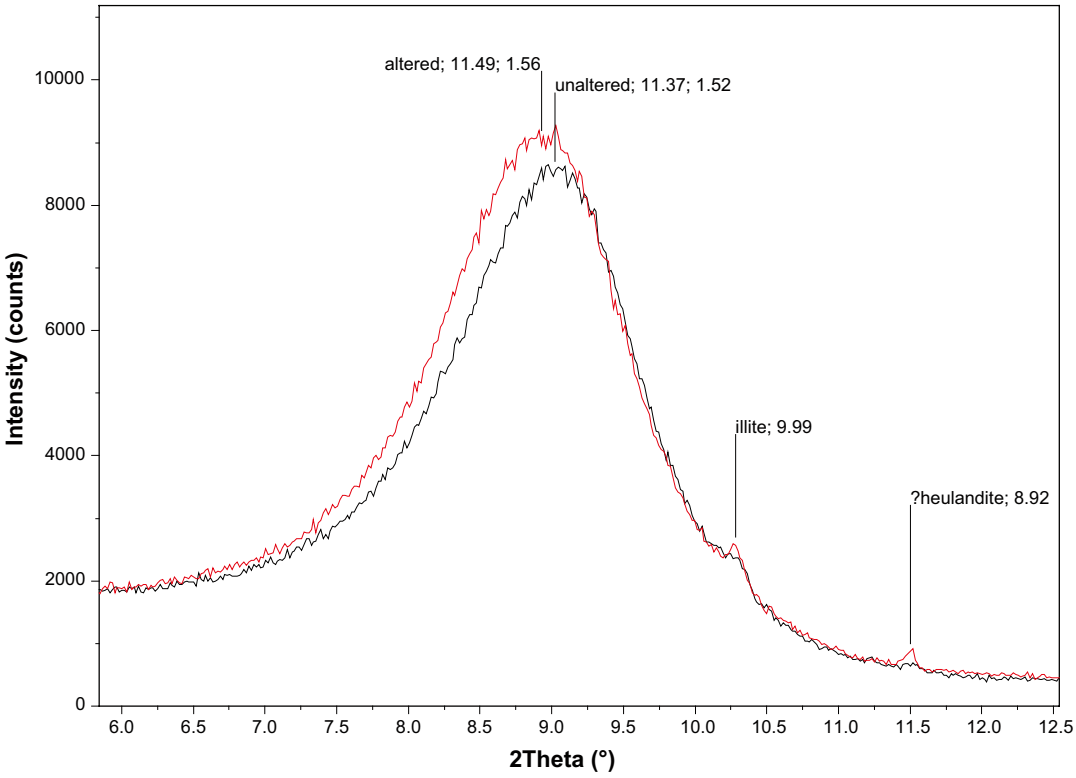

Figure 4-27. *Low angle section of air-dry oriented mount XRD traces to illustrate increase in spacing (Å) and FWHM for the montmorillonite* $\mathbf{d}_{001}$ *peak in altered material (red trace) compared to the 'unaltered' material (black trace), Experiment NFC 16, sample 16a.*

Table 4-1. Summary of random orientation mount XRD analyses.

SERCO sample code	BGS sample code	Description	Subsample	Mineralogy	Montmorillonite	
					d_{001} (Å)	d_{060} (Å)
12a	MPLM561	Grey-green bentonite disc with corrosion products on one side due to contact with iron coupon	_1 'unaltered'	montmorillonite, quartz, halite, cristobalite, albite, K-feldspar, pyrite	12.74	1.4966
12b	MPLM562	Bentonite with steel wires and corrosion on opposite side	_1 'unaltered'	montmorillonite, quartz, halite, albite, K-feldspar, 'mica', pyrite	12.72	1.4957
			_2 wire altered	montmorillonite, quartz, halite, albite, K-feldspar, 'mica', pyrite	12.88	1.4969
12c	MPLM563	Bentonite with steel wires, pervasively stained with corrosion products	wire altered	montmorillonite, quartz, halite, cristobalite, albite, K-feldspar, 'mica', pyrite	12.88	1.4965
16a	MPLM565	Bentonite, half grey-green, half with steel wires, half pervasively stained with corrosion products	_1 'unaltered'	montmorillonite, quartz, halite, cristobalite, albite, K-feldspar, calcite, pyrite, gypsum	12.73	1.4968
			_2 wire altered	montmorillonite, quartz, halite, albite, K-feldspar, 'mica', pyrite, ?heulandite	12.78	1.4966
			_3 wire scraping	montmorillonite, quartz, halite, albite, aragonite, cristobalite, 'mica', ?heulandite	12.86	na
16b	MPLM566	Bentonite with steel wires, pervasively stained with corrosion products	_1 wire altered	montmorillonite, quartz, halite, albite, K-feldspar, aragonite, 'mica'	12.85	1.4966
			_2 wire	iron, quartz	na	na
17a	MPLM567	Bentonite with steel wires, pervasively stained with corrosion products	_1 wire altered	montmorillonite, quartz, halite, cristobalite, albite, K-feldspar, 'mica'	12.78	1.4962
			_2 wire scraping	montmorillonite, quartz, albite, aragonite, cristobalite, K-feldspar, 'mica'	12.89	na
17b	MPLM568	Grey-green bentonite disc	_1 'unaltered'	montmorillonite, quartz, halite, cristobalite, albite, K-feldspar, calcite, pyrite, gypsum, goethite	12.77	1.4972
17c	MPLM569	Bentonite with steel wires, pervasively stained with corrosion products	_1 wire altered	montmorillonite, quartz, halite, cristobalite, albite, K-feldspar, 'mica', pyrite	12.76	1.4961
			_2 wire scraping	montmorillonite, quartz, albite, aragonite, cristobalite, 'mica', magnetite	12.84 + 14.09	1.4982

Table 4-2. Summary of oriented mount XRD analyses.

SERCO sample code	BGS sample code	Description	Subsample	Montmorillonite		
				d_{001} (Å)	d_{001} FWHM	d_{002}/d_{003}
12a	MPLM561	Grey-green bentonite disc with corrosion products on one side due to contact with iron coupon	_1 'unaltered'	11.56	1.46	0.68
			_2 iron coupon alteration	11.83	1.49	0.78
12b	MPLM562	Bentonite with steel wires and corrosion on opposite side	_1 'unaltered'	11.61	1.47	0.73
			_2 wire altered	11.85	1.43	0.73
12c	MPLM563	Bentonite with steel wires, pervasively stained with corrosion products	wire altered	11.90	1.47	0.70
16a	MPLM565	Bentonite, half grey-green, half with steel wires, half pervasively stained with corrosion products	_1 'unaltered'	11.37	1.52	0.73
			_2 wire altered	11.49	1.56	0.68
16b	MPLM566	Bentonite with steel wires, pervasively stained with corrosion products	_1 wire altered	11.70	1.56	0.76
17a	MPLM567	Bentonite with steel wires, pervasively stained with corrosion products	_1 wire altered	11.77	1.65	0.74
17b	MPLM568	Grey-green bentonite disc	_1 'unaltered'	11.23	1.64	0.81
17c	MPLM569	Bentonite with steel wires, pervasively stained with corrosion products	_1 wire altered	11.47	1.68	0.76

KEY

FWHM = full XRD peak width at half maximum

d_{002}/d_{003} = XRD peak intensity ratio from glycol-solvated trace.

4.3 Cation exchange and exchangeable cation characteristics

The results of the CEC and exchangeable cation determinations for altered bentonite from the bentonite-steel wire zone in each of the experiments, and background unaltered bentonite from the end of the cell in Experiment 17 are summarised in Table 4-3. These data are plotted in Figure 4-28 to show the variation in CEC and exchangeable cation characteristics in relation to the position of the bentonite sample within the experiments.

Very subtle differences can be seen in the CEC and exchangeable cation chemistry between the background unaltered bentonite and bentonite from the zone of steel wire alteration. Because of the very small dataset, any conclusions drawn from these results should be treated cautiously. However, what seems to be apparent in all three experiments is a slight decrease (10–15 %) in total CEC in the bentonite from bentonite-steel wire zone compared to the background bentonite reference sample (17b). Surprisingly, this seems to be more marked at the interface between the altered and unaltered bentonite, rather than within the 'core' of the steel wire alteration region. This is mirrored by variations in the exchangeable Ca and Na, although proportionally the greatest differences are seen for Ca. Exchangeable Mg on the other hand appears to show a continual slight decrease from the 'background' bentonite, through the interface region, and into the 'core' of the steel wire alteration zone, decreasing by up to 50 %. Exchangeable Fe is very small, but appears to increase towards the 'core' of the alteration region, compared to the background sample. Potassium, although a very minor component, may also show a slight increase within the alteration zone.

Table 4-3. Cation exchange capacity (by titration) and exchangeable cations (determined by ICP-AES) data for reacted bentonite samples.

Serco sample code	BGS sample code	CEC by titration	Exchangeable cation analysis by ICP-AES*					
			Ca	Fe	K	Mg	Na	Total
		meq/100g	meq/100g	meq/100g	meq/100g	meq/100g	meq/100g	meq/100g
12b	MPLM 562	87.0	18.3	0.8	1.9	9.3	86.8	117.1
12c	MPLM 563	99.3	21.5	1.6	2.3	8.9	100.1	134.4
16a	MPLM 565	92.1	22.1	0.9	1.6	10.2	87.1	121.9
16b	MPLM 566	98.4	22.2	1.7	2.5	8.1	92.7	127.2
17a	MPLM 567	93.2	19.9	1.4	2.2	10.5	95.9	129.9
17b	MPLM 568	103.9	27.0	0.2	2.1	12.4	99.7	141.4
17c	MPLM 569	99.6	20.7	2.3	2.5	10.2	104.6	140.3

Serco sample code	BGS sample code	Ca mg/kg	Fe mg/kg	K mg/kg	Mg mg/kg	Na mg/kg
12b	MPLM 562	3,666	234	739	1,132	19,948
12c	MPLM 563	4,314	450	887	1,084	23,016
16a	MPLM 565	4,427	242	625	1,241	20,017
16b	MPLM 566	4,446	479	969	989	21,319
17a	MPLM 567	3,996	393	873	1,280	22,040
17b	MPLM 568	5,410	43	826	1,512	22,910
17c	MPLM 569	4,153	638	980	1,243	24,054

Note: *concentration data for exchangeable cations are presented both as meq/100g and in mg/kg.

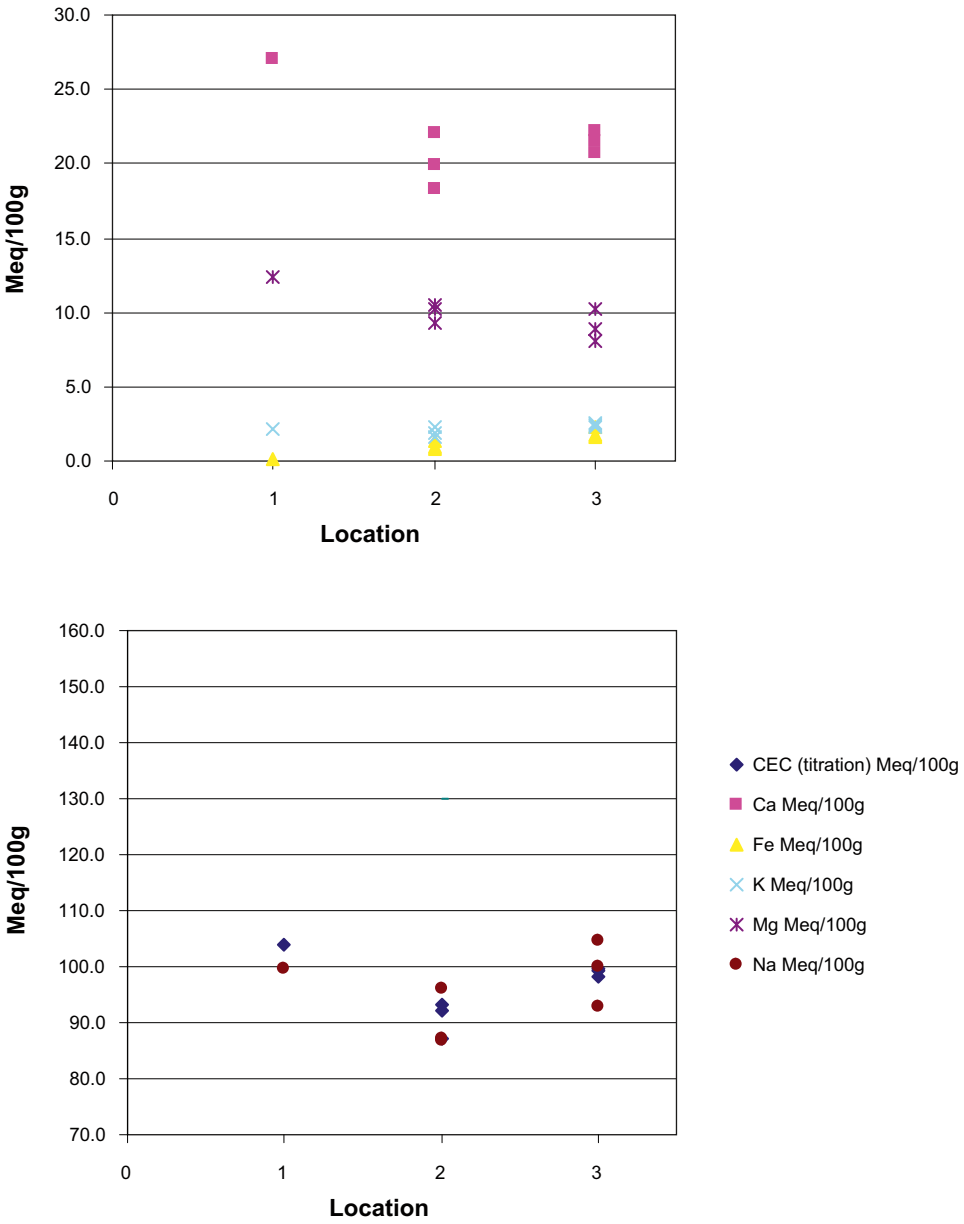

Figure 4-28. *Plots showing the variation in CEC and exchangeable cation chemistry in bentonite, in relation to the location of the subsample within the reacted bentonite cylinders. Location 1 – unreacted background bentonite (subsample 17b); Location 2 – outer margin of the bentonite-steel wire alteration zone; Location 3 – central 'core' region of the bentonite-steel wire alteration zone.*

4.4 Sequential chemical extraction analysis

4.4.1 Data processing

The data from the deionised water extraction was not used due to difficulties in separating fines from the extraction solution. The data processing was carried by combining the extraction data (excluding the deionised water extractions) for subsample 12c from Experiment NFC12, subsample 16b (extracted in duplicate) from Experiment NFC16, and subsamples 17b and 17c from Experiment NFC17. The element data used for each extract was Al, Ba, Ca, Cr, Cu, Fe, K, Mg, Mn, Na, Ni, P, Pb, S, Si, Sr and Zn, giving rise to data matrix consisting of 60 rows (the extractions) and 17 columns (the elements). Sample NFC17b represents background unreacted bentonite containing no steel wire. The remaining samples all contained reacted bentonite from close proximity to corroded steel wire in each of the experiments.

The data processing identifies distinct physico-chemical components in the bentonite samples identified by their chemical composition and their ease of extraction.

The processing identified 11 components. The name of each component is made up of those elements that make up more than 10% of its composition (listed in order of magnitude). The error bars on the profiles are derived from the root mean square fit of the modelled data to the original data set. Less significance should be given to components whose error bars are large compared to the total amount of material extracted. The component names and the tentative assignments, based on the acid strength at which the component was extracted and mineralogical knowledge of the sample, are given in Table 4-4 and Table 4-5.

Figure 4-29 and Figure 4-30 summarise the extraction profiles of the 11 components. The extracts 1 to 60 are shown on the x axis. Reading along the x axis from left to right, extraction profiles for NFC17b, NFC17c, NFC12c, NFC16b and a duplicate of NFC16b, respectively, are observed with increasing acid concentration within each profile. The y-axis of each of the plots gives the total solids extracted in mg kg^{-1} for the component in question.

Examination of Figure 4-29 and Figure 4-30 shows that three of the components only appear in the samples containing steel wire. These are the Ca-Mg, the Na-Fe and the Fe components. Since they only occur in the samples containing steel wire it is likely that they have been formed due to its presence.

Table 4-4. Component names and tentative assignments.

Component name	Tentative assignment
Al-S-Si	clay lattice
Ca-Fe-Mg	clay lattice
Ca-Mg*	carbonates
Na-Fe*	ion-exchangeable
Na-S	–
Ca-Na	–
Ca-Si-S-P	clay lattice
Fe*	steel wire corrosion products
Fe-Si	Fe oxides
Na 1	ion-exchangeable
Na 2	ion-exchangeable

Table 4-5. Relationship between extract number acid strength and sample name.

Extract no.	Acid conc.	SERCO sample/ subsample code	BGS sample code	Extract no	Acid conc.	SERCO sample/ subsample code	BGS sample code
1	0.01M	NFC17b	MPLM568	31	0.5M	NFC12c	MPLM563
2	0.01M	NFC17b	MPLM568	32	0.5M	NFC12c	MPLM563
3	0.05M	NFC17b	MPLM568	33	1.0M	NFC12c	MPLM563
4	0.05M	NFC17b	MPLM568	34	1.0M	NFC12c	MPLM563
5	0.1M	NFC17b	MPLM568	35	5.0M	NFC12c	MPLM563
6	0.1M	NFC17b	MPLM568	36	5.0M	NFC12c	MPLM563
7	0.5M	NFC17b	MPLM568	37	0.01M	NFC16b	MPLM566
8	0.5M	NFC17b	MPLM568	38	0.01M	NFC16b	MPLM566
9	1.0M	NFC17b	MPLM568	39	0.05M	NFC16b	MPLM566
10	1.0M	NFC17b	MPLM568	40	0.05M	NFC16b	MPLM566
11	5.0M	NFC17b	MPLM568	41	0.1M	NFC16b	MPLM566
12	5.0M	NFC17b	MPLM568	42	0.1M	NFC16b	MPLM566
13	0.01M	NFC17c	MPLM569	43	0.5M	NFC16b	MPLM566
14	0.01M	NFC17c	MPLM569	44	0.5M	NFC16b	MPLM566
15	0.05M	NFC17c	MPLM569	45	1.0M	NFC16b	MPLM566
16	0.05M	NFC17c	MPLM569	46	1.0M	NFC16b	MPLM566
17	0.1M	NFC17c	MPLM569	47	5.0M	NFC16b	MPLM566
18	0.1M	NFC17c	MPLM569	48	5.0M	NFC16b	MPLM566
19	0.5M	NFC17c	MPLM569	49	0.01M	NFC16b	MPLM566
20	0.5M	NFC17c	MPLM569	50	0.01M	NFC16b	MPLM566
21	1.0M	NFC17c	MPLM569	51	0.05M	NFC16b	MPLM566
22	1.0M	NFC17c	MPLM569	52	0.05M	NFC16b	MPLM566
23	5.0M	NFC17c	MPLM569	53	0.1M	NFC16b	MPLM566
24	5.0M	NFC17c	MPLM569	54	0.1M	NFC16b	MPLM566
25	0.01M	NFC12c	MPLM563	55	0.5M	NFC16b	MPLM566
26	0.01M	NFC12c	MPLM563	56	0.5M	NFC16b	MPLM566
27	0.05M	NFC12c	MPLM563	57	1.0M	NFC16b	MPLM566
28	0.05M	NFC12c	MPLM563	58	1.0M	NFC16b	MPLM566
29	0.1M	NFC12c	MPLM563	59	5.0M	NFC16b	MPLM566
30	0.1M	NFC12c	MPLM563	60	5.0M	NFC16b	MPLM566

The ‘Fe component’ is obviously the Fe originating from oxidation of the steel wire. Table 4-6 shows that the total Fe content of the starting material is on average c.8 times higher in the steel wire containing samples. The proportion of Fe extracted by the sequential acid extraction in samples containing steel wire is much higher (c.37 to 56% compared to 10%) showing that the Fe is in a much more acid soluble form than in the ‘clean’ bentonite (steel wire corrosion products compared with Fe from the clay fabric). The ‘Fe component’ identified by the CISED analyses (Table 4-4) makes up a large proportion of the total Fe extracted (58 to 80%, Table 4-6).

The ‘Ca-Mg component’ is likely to be derived from dissolution of carbonates as it is dissolved at relatively low acid concentrations and seems to have been formed as a by-product of the wire corrosion.

The Na-Fe component may suggest the presence of Fe as well as Na in the cation exchange sites within the clay suggesting that some of the Fe from the wire has been mobilised into the interlayer sites.

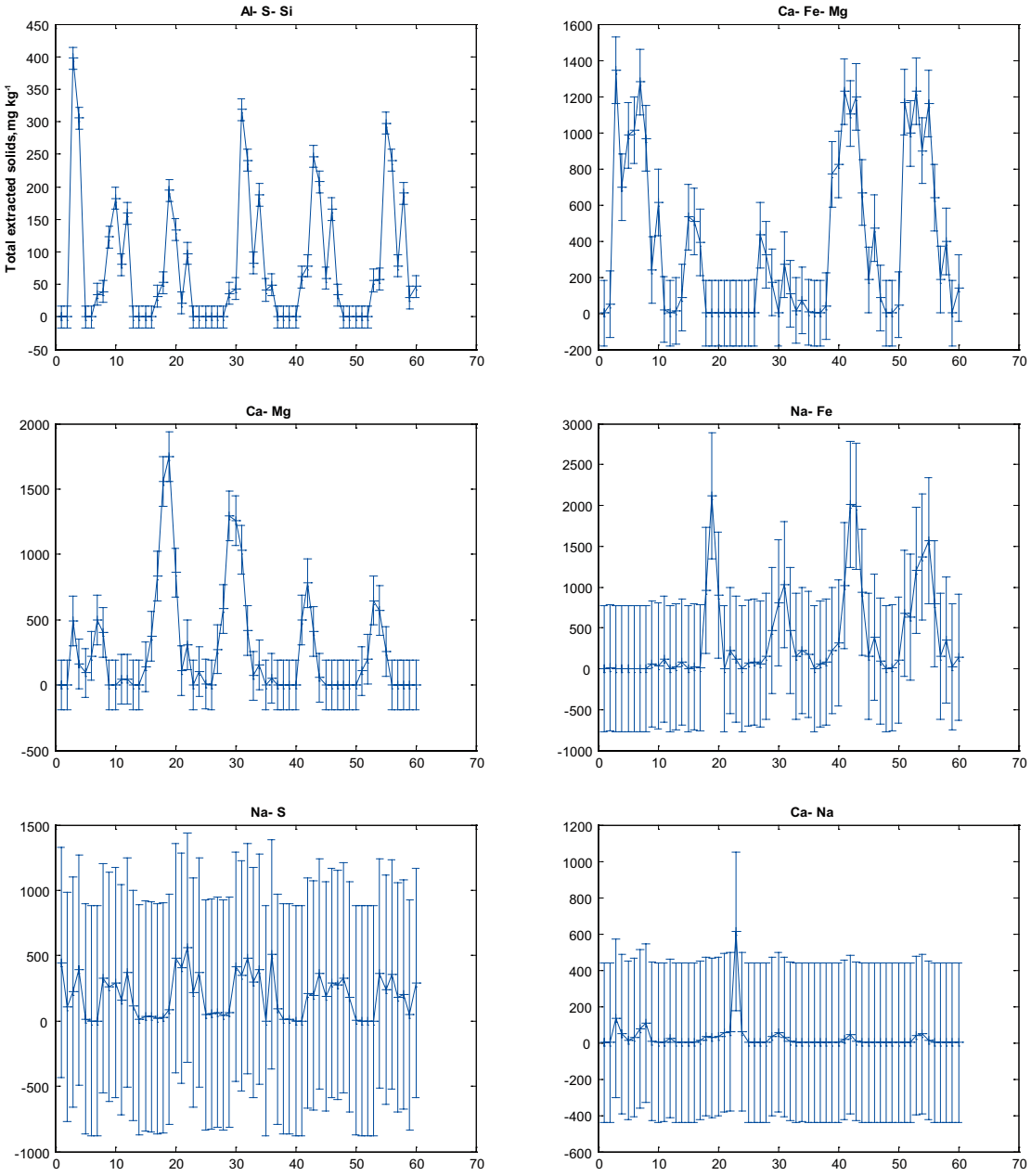

Figure 4-29. *Component profiles for Al-S-Si, Ca-Fe-Mg, Ca-Mg, Na-Fe, Na-S, Ca-Na.*

Table 4-6. Iron contents of samples and sequential chemical extracts.

SERCO sample/ subsample code	BGS sample code	Total Fe in material (mg/kg)	Total Fe extracted (mg/kg)	Proportion extracted (%)	Fe content of CISED 'Fe component' (mg/kg)	Proportion of total Fe extracted (%)
NFC17b	MPLM568	21,457	2,188	10.2	118	5.4
NFC17c	MPLM569	46,687	26,030	55.8	20,905	80.3
NFC12c	MPLM563	41,487	15,414	37.2	11,017	71.5
NFC16b	MPLM566	38,958	16,197	41.6	9,346	57.7
NFC16b (duplicate)	MPLM566	38,958	14,335	36.8	8,339	58.2

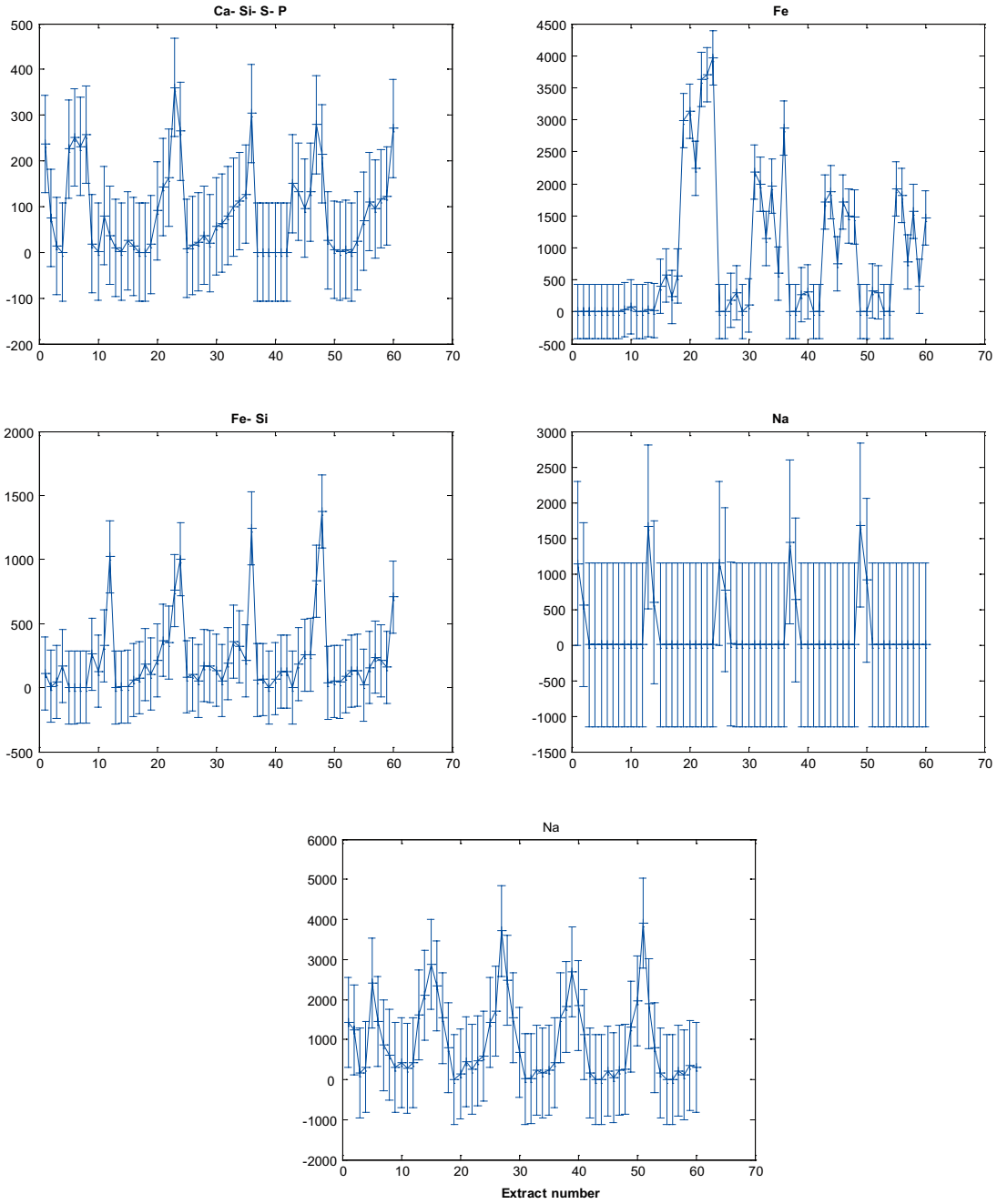

Figure 4-30. *Component profiles for Ca-Si-S-P, Fe, Fe-Si, Na1, Na2.*

5 Discussions and conclusions

5.1 Background mineralogical characteristics of MX-80 bentonite

XRD analysis in this study reveals that the 'unaltered', grey bentonite shows a similar composition to that previously described for MX-80 /e.g. Madsen 1998/. It is predominantly composed of Na/K-montmorillonite together with minor-trace amounts of quartz, halite, cristobalite, feldspar (albite and K-feldspar) and pyrite, sometimes with traces of undifferentiated mica species ('mica', possibly including muscovite, biotite, illite, illite/smectite etc), calcite, gypsum and goethite. Small quantities of a zeolite-group mineral, probably heulandite were also detected. The halite detected almost certainly results from evaporation of the experimental brine solution. An annotated example random powder XRD trace is shown in Figure 4-23.

Detailed petrographical analysis shows that the feldspars and apatite are present as angular silt and sand sized grains, which show little alteration. Petrographical analysis also identified trace amounts of calcite disseminated throughout the bentonite. It occurs as irregular patches and angular grains within hydrated 'clasts' of the original granular bentonite, and is seen in both background and reacted bentonite samples. The calcite shows no evidence of dissolution in the reacted bentonite samples.

Pyrite was observed to be present as framboidal (spherical) microcrystalline aggregates of submicron crystallites. The pyrite appeared to be fresh in both the background and altered bentonite samples.

5.2 Bentonite alteration characteristics

5.2.1 Clay mineral alteration

Evidence from XRD

Analysis of randomly oriented clay mineral XRD mounts shows a mean d_{060} dimension of 1.4966 Å (range of values 1.4957 to 1.4972 Å) for the background 'unaltered' grey bentonite subsamples. This indicates that the smectite-group mineral can be classified as dioctahedral and most likely is a montmorillonite species. A similar mean d_{060} dimension of 1.4965 Å and range of values (1.4961 to 1.4969 Å) for the altered bentonite subsamples indicates that the smectite-group mineral has remained dioctahedral following reaction.

Random mount measurements indicate that the montmorillonite in the 'unaltered' grey bentonite subsamples displays a mean d_{001} spacing of c.12.74 Å (range of values 12.72 to 12.77 Å) suggesting that monovalent (Na/K) cations dominate the smectite interlayer cations. The montmorillonite in the altered bentonite subsamples displays a slightly larger mean d_{001} spacing of c.12.82 Å (range of values 12.76 to 12.88 Å). Such an increase in the smectite c-axis dimension may indicate the replacement of some of the monovalent (Na/K) interlayer cations with larger divalent cations. As the experiment involves corrosion of steel wires, these divalent cations may be Fe.

FWHM measurements for the montmorillonite d_{001} peak from the random mounts produces a mean value of 0.59 ± 0.03 Δ°2θ for the 'unaltered' bentonite samples. Similar measurements for the altered bentonite produces a larger mean value of 0.64 Δ°2θ (range 0.59 to 0.73 Δ°2θ) suggesting a smaller crystallite size distribution for the reacted bentonite.

Subsamples taken from the surface of the corroding wires have a mean d_{001} spacing of c.12.88 Å (range of values 12.86 and 12.89 Å) and a mean FWHM of 0.89 Δ°2θ (range 0.86 and 0.91 Δ°2θ). This would seem to suggest that the montmorillonite in close proximity to the corroding wires has undergone further divalent ion (possibly Fe) exchange with the originally monovalent interlayer cations and a further reduction in crystallite size distribution when compared with the unaltered bentonite.

Oriented clay mineral XRD mounts similarly show an increase in the spacing of the montmorillonite air-dry d_{001} spacing of c.11.5 Å (range of values 11.2 to 11.6 Å) for the 'unaltered' bentonite to c.11.7 Å (range of values 11.4 to 11.9 Å) for the altered bentonite. It is unclear why the oriented mount d_{001} spacing is consistently c.1 Å less than the same spacing measured on the random mounts of similar samples. A possible reason for such behaviour might be that further Na exchange has occurred between the montmorillonite and halite precipitated on its surface during the hydration necessary for oriented mount preparation and so reduced the measured d_{001} spacing. Alternatively, the oriented mounts may have achieved a more stable, dehydrated state following overnight air-drying prior to analysis whereas the random mounts were run immediately after preparation to prevent further oxidation effects.

The width of the d_{001} peak also increases from the 'unaltered' (mean FWHM 1.52 Δ°2θ) to the altered bentonite and (1.55 Δ°2θ) suggesting a reduction in crystallite size distribution.

The d_{002} / d_{003} values for the montmorillonite in the 'unaltered' bentonite subsamples range from 0.99 to 1.25 (mean 1.11) while those for the altered bentonite subsamples show slightly increased values of 1.04 to 1.48 (mean 1.17). Such an increase suggests an increase in the total number of electrons in the octahedral sheet of the altered bentonite, possibly as a result of Fe substitution. This might indicate partial alteration and conversion of dioctahedral montmorillonite to an iron rich dioctahedral smectite such as nontronite. A similar effect might also be expected if Fe^{2+} or Fe^{3+} from the corroding steel had displaced interlayer cations in the smectite and this had subsequently converted to form an Fe-rich octahedral layer. This would have the overall effect of increasing the apparent Fe-substitution within the octahedral layer of the bulk of the smectite, and might be an alternative explanation for the increase in the d_{002} / d_{003} values for the montmorillonite component in the altered bentonite.

The broad, low intensity superlattice peak at c.21.8 Å on the air-dry XRD trace which expands to c.31.4 Å on glycolation could not be definitively identified but is present in both 'unaltered' and altered subsamples. It may suggest the presence of trace amounts of an interlayered smectite-bearing phase in the original bentonite.

Petrographical evidence

Detailed BSEM-EDXA petrography revealed significant interaction between Fe released as a result of the corrosion of steel wires and the adjacent clay matrix of the enclosing bentonite, in all three Serco Assurance experiments (NFC12, NFC16 and NFC17). Experiments NFC12 and NFC17 displayed significantly more alteration than Experiment NFC16. However, all three show broadly the same kind of alteration effect.

Both BSEM images and X-ray element mapping show an alteration halo around the corroded steel wires in the bentonite. The bentonite within this halo has significantly enhanced concentrations of Fe, which is of the order of several wt.% adjacent to the metal decreasing to background levels over distances ranging between 0.05 to 0.1 mm (Experiment NFC16) and up to 1 mm (Experiment NFC17) from the wire. The greatest penetration of Fe into the bentonite matrix occurs along hairline microfractures that radiate outwards from the corroding metal. /Smart et al. 2006/ also recorded a slight enhancement of Fe in bentonite adjacent to corroding wires in early preliminary investigations. Their observations noted iron enrichment over distances varying between 0.1 and 1.5 mm from the metal. However, the alteration haloes were much less obvious and more diffuse than those observed in the experiments in this study.

Close examination shows that whilst a thin layer of discrete iron oxide or iron oxyhydroxide (these cannot be differentiated by BSEM-EDXA) may be present as very fine coatings on the walls of these microfractures, no discrete iron oxide phase (other than primary particles of accessory magnetite and ilmenite originally present in the bentonite) could be discerned in the clay matrix within the limits of spatial resolution of the BSEM petrographical analysis (i.e. better than 0.1 μm). The matrix clay particles within the Fe-enriched halo appear brighter under BSEM than in the unaltered clay, suggesting that the clay minerals have become enriched in Fe. This is consistent with the tentative interpretations from the XRD analyses that: either Fe substitution has occurred within the octahedral layer; or that Fe may has displaced Na^+ and Ca^{2+} from the exchangeable cation interlayer, possibly resulting in the formation of additional Fe-rich octahedral layers. These clay alteration features might be indicative of an early stage in the mechanism of conversion of dioctahedral montmorillonite to an Fe-rich dioctahedral smectite such as nontronite). Alternatively it may reflect partial alteration of the montmorillonite to chlorite (berthierine), or to a mixed-layer chlorite-smectite, as proposed by /Wilson et al. 2006a/ as a potential alteration process, and has been observed in experimental studies at much higher temperatures (250°C) where montmorillonite had been reacted with metallic iron and $FeCl_2$ solutions /Wilson et al. 2006b/.

5.2.2 Other mineralogical alteration

The altered, pervasively-stained bentonite in contact with the corroded steel wires has a generally similar mineralogy to the 'unaltered' bentonite. However, aragonite was detected in the altered bentonite material (sample 16b) and material removed directly from the surface of the steel wires. Although traces of calcite are present, aragonite was not detected in the 'unaltered' background bentonite material suggesting that aragonite has formed during interaction with the steel wires.

Detailed petrographical analyses reveal that the aragonite has formed as a result of the concentration of Ca in the bentonite immediately adjacent to the corroding iron, and along the leading edge of diffuse fronts of Fe within the halo of altered bentonite around the steel wires. The aragonite occurs as fine grained thin alteration fringes or layers (10–30 μm thick) replacing the bentonite at the interface with the corroding steel, or fine acicular crystals that line open fractures within the bentonite that radiate from the corroding wire surface.

Since the porefluid used in the experiments did not contain Ca, and there is no petrographical evidence for the dissolution of discrete Ca minerals (calcite, apatite, feldspar) originally present in the bentonite, then, the Ca must have been derived from the exchangeable cation sites in montmorillonite. Although MX-80 is described as a Na-saturated bentonite, the presence of a significant amount of exchangeable Ca is reported in the literature /Herbert and Moog 1999, Bradbury and Baeyens 2003, Carlson et al. 2006, Smart et al. 2006/, and up to 5,410 mg/kg was recorded in this study from the background 'unaltered' bentonite. The petrographical evidence indicates that Fe from the corroding steel has displaced the Ca^{2+} from the exchangeable cation interlayer sites in the montmorillonite. The pattern of Ca distribution shows that the Ca has concentrated in several bands around the steel wires. Initially, Ca has been displaced from bentonite at the interface with the steel, or it migrated towards the corroding metal as Fe has diffused into the bentonite. In addition, later bands of aragonite formed as more Ca^{2+} was displaced from the bentonite and was concentrated at the leading edges of the diffusive Fe fronts as Fe migrated away from the wire and into the bentonite matrix. These observations are consistent with potential mechanism for bentonite alteration under anoxic conditions, described previously by /Kamei et al. 1999/ and /Idemitsu et al. 2003/, involving substitution of interlayer cations such as Na^+ and Ca^{2+} by Fe^{2+} produced by iron corrosion.

5.2.3 Change in cation exchange properties

The CEC and exchangeable cation analyses show a subtle decrease in CEC, Ca and Na within the altered steel-wire-bentonite zone in each experiment. A small amount of exchangeable Fe was also found in the matrix of the bentonite from this region. These changes represent the overall cation exchange characteristics of the relatively coarse-scale bulk sample that was analysed. However, it is likely that the changes within the narrow bentonite alteration haloes around the corroding steel wire are much more significant. Unfortunately, these are on too fine a scale to sub-sample for CEC and exchangeable cation analysis. Nevertheless, the observations are consistent with petrographical analyses, which show that exchangeable Ca^{2+} has been displaced by Fe in the reacted bentonite (discussed in Section 5.2.2).

5.2.4 Bentonite shrinkage and swelling characteristics

It was noted during petrographical examination of the thin sections that the shrinkage behaviour of the clay matrix varied within the steel wire-bentonite zone. The bentonite that was strongly enriched in Fe close to the corroding wires displayed significantly different shrinkage behaviour to the lower-Fe bentonite matrix further away from the corroding wires. Shrinkage of the bentonite had occurred in two stages:

1. Early shrinkage of the clay matrix within the Fe-rich alteration haloes immediately adjacent to the corroding steel. This produced microfractures with apertures up to 50 µm, although in most cases, fracture apertures range between <0.5–10 µm. These fractures clearly formed during the course of the experiment, as they are closely associated with the enrichment of Fe in the clay walls and the precipitation of thin coatings of aragonite produced as a result of the displacement of exchangeable Ca^{2+} by Fe from the montmorillonite interlayer cation sites. Similarly, the precipitation of iron oxide coatings on the walls of these fractures also illustrates that these fractures formed in situ during the course of the experiments.

2. Later unmineralised microfractures cross cutting, and sometimes accentuating or re-utilising, the earlier formed microfractures. These most probably formed post-experimentation, as a result of clay shrinkage during sample drying and epoxy-resin impregnation for thin section preparation.

The petrographical observations show that the altered bentonite that has been significantly enriched with Fe from steel corrosion, has a tendency to show significantly reduced shrinkage on sample drying than the unaltered bentonite. Conversely, this would suggest that the reacted and altered clay will also have less ability to swell on hydration with water. Although XRD indicates that the smectite in the reacted bentonite is dioctahedral, possibly the original montmorillonite may have been converted to Fe-rich dioctahedral smectite (e.g. nontronite) within the alteration haloes. /Wilson 2006b/ showed that one of the effects of altering montmorillonite to Fe-rich smectite is to reduce its expandability. This may explain the shrinkage and reduction in expandability observed in this petrographical study of the altered bentonite from the NF-PRO experiments.

The early formed fractures may have represented potentially important pathways for gas and solute transport during the course of the experiments. The irreversible shrinkage of the bentonite, as a result of interaction with Fe released from corroding iron or steel may therefore be significant in evaluating the long-term behaviour of the bentonite seal and the transport of gas and solutes around corroding waste canisters emplaced in bentonite backfill.

5.3 Steel corrosion

A poorly crystalline iron oxyhydroxide phase, tentatively identified by XRD as åkaganeite [Fe(O,OH,Cl)] was found in iron corrosion products taken directly from the steel wire surfaces in all three experiments. Aragonite was also detected in all samples but on the basis of petrographical evidence this is most probably derived from attached altered bentonite.

Magnetite was detected as a surface corrosion product in sample 17c. However, the observation that the iron oxide corrosion products from all three experiments are magnetic would suggest that magnetite is a reaction product in all three cases. The formation of magnetite as a corrosion product of steel or iron might be expected under the anoxic conditions of these experiments.

References

Bascomb C L, 1964. Rapid method for the determination of cation-exchange capacity of calcareous and noncalcareous soils. Journal of the Science of Food and Agriculture, 12, 821–823.

Bradbury M H, Baeyens B, 2003. Porewater chemistry in compacted re-saturated MX-80 bentonite. Journal of Contaminant Hydrology, 61, 329–338.

Carlson L, Karnland O, Oversby V M, Rance A P, Smart N R, Snellman M, Vahanen M, Werme L O, 2006 (in press). Experimental studies of the interactions between anaerobically corroding iron and bentonite. Physics and Chemistry of the Earth, 32, 334–345.

Cave M R, Milodowski A E, Friel E N, 2004. Evaluation of a method for Identification of host physico-chemical phases for trace metals and measurement of their solid-phase partitioning in soil samples by nitric acid extraction and chemometric mixture resolution. Geochemistry: Exploration, Environment, Analysis, 4, 71–86.

Gillespie M R, Leader R U, Higgo J J W, Harrison I, Hards V L, Gowing C J B, Vickers B P, Boland M P, Morgan D J, 2000a. CEC & Kd determination in landfill performance evaluation: a review of methodologies and preparation of standard materials for laboratory analysis. Environment Agency R &D Technical Report, P340.

Gillespie M R, Leader R U, Higgo J J W, Harrison I, Hards V L, Gowing C J B, Vickers B P, Boland M P, Morgan D J, 2000b. CEC & Kd determination in landfill performance evaluation: a review of methodologies and preparation of standard materials for laboratory analysis. Environment Agency R &D Project Record, P1/254/01.

Gillespie M R, Kemp S J, Vickers B P, Waters C, Gowing C J, 2001. Cation-exchange capacity (CEC) of selected lithologies from England, Wales and Scotland. Environment Agency R&D Technical Report, P2-222/TR.

Goldstein J I, Newbury D E, Echlin P, Joy D C, Fiori C, Lifshin E, 1981. Scanning Electron Microscopy and X-Ray Microanalysis. Plenum Press, New York.

Herbert H-J, Moog H C, 1999. Cation exchange, interlayer spacing, and water content of MX-80 bentonite in high molar saline solutions. Engineering Geology, 54, 55–65.

Idemitsu K, Yano S, Xia X, Kikuchi Y, Inagaki Y, Arima T, 2003. Migration behaviour of iron in compacted bentonite under reducing condition using electromigration. Material Research Society Symposium Proceedings, 757, II3.7.1–II3.7.8.

Kamei G, Oda C, Mitsui S, Shibata M, Shinozaki T, 1999. Fe(II)-Na ion exchange at interlayers of smectite: adsorption-desorption experiments and a natural analogue. Engineering Geology, 54, 15–20.

Kostka J E, Wu J, Nealson K H, Stuki J, 1999. The impact of structural Fe(III) reduction by bacteria on the surface chemistry of smectitic clay minerals. Geochemica et Cosmochimica Acta, 63, 3705–3713.

Madsen F T, 1998. Clay mineralogical investigations related to nuclear waste disposal. Clay Minerals, 33, 109–129.

Moore D M, Reynolds R C, 1997. X-Ray Diffraction and the Identification and Analysis of Clay Minerals, Second Edition. Oxford University Press, New York.

Reynolds R C, Reynolds R C, 1996. Description of Newmod-for-Windows™. The calculation of one-dimensional X-ray diffraction patterns of mixed layered clay minerals. R C Reynolds Jr., 8 Brook Road, Hanover, NH.

Smart N R, Carlson L, Hunter F M I, Karnland O, Pritchard A M, Rance A P, Werme L O, 2006. Interactions between iron corrosion products and bentonite. Serco Assurance Report, SA/EIG/12156/C001.

Stuki J W, Low P F, Roth C B, Golden D C, 1984. Effects of oxidation state on octahedral iron on clay swelling. Clays and Clay Minerals, 32, 357–362.

Wilson J, Savage D, Cuadros J, Shibata M, Ragnarsdottir K V, 2006a. The effect of iron on montmorillonite stability. (I) Background and thermodynamic consideration. Geochimica et Cosmochimica Acta, 70, 306–322.

Wilson J, Cressey G, Cressey B, Cuadros J, Ragnarsdottir K V, Savage D, Shibata M, 2006b. The effect of iron on montmorillonite stability. (I) Experimental investigations. Geochimica et Cosmochimica Acta, 70, 306–322.

ISSN 1404-0344
CM Gruppen AB, Bromma, 2009